The Astrophysical Journal, 994:181 (19pp), 2025 December 1 https://doi.org/10.3847/1538-4357/ae0a4b

BASS. LIV. Physical Properties of AGN-hosting Galaxy Mergers from Multiwavelength SED Fitting

Marco Troncoso[1], Ezequiel Treister[2], Alejandra Rojas[3], Médéric Boquien[4], Franz Bauer[2], Michael J. Koss[5], Roberto J. Assef[6], Miguel Parra Tello[1], Ignacio del Moral-Castro[1], Claudio Ricci[6], Sophia Dai[7], Kyuseok Oh[8], Federica Ricci[9], Alessandro Peca[5], C. Megan Urry[10], Kriti Kamal Gupta[11,12], Giacomo Venturi[13,14], Matilde Signorini[15], Richard Mushotzky[16], and David Sanders[17]

[1] Instituto de Astrofísica, Facultad de Física, Pontificia Universidad Católica de Chile, Av. Vicuña Mackenna 4860, 782-0436 Macul, Santiago, Chile; marco.troncoso@uc.cl
[2] Instituto de Alta Investigación, Universidad de Tarapacá, Casilla 7D, Arica, Chile
[3] Departamento de Física, Universidad Técnica Federico Santa María, Vicuña Mackenna 3939, San Joaquín, Santiago de Chile, Chile
[4] Université Côte d'Azur, Observatoire de la Côte d'Azur, CNRS, Laboratoire Lagrange, 06000, Nice, France
[5] Eureka Scientific, 2452 Delmer Street, Suite 100, Oakland, CA 94602-3017, USA
[6] Instituto de Estudios Astrofísicos, Facultad de Ingeniería y Ciencias, Universidad Diego Portales, Av. Ejército Libertador 441, Santiago, Chile
[7] National Astronomical Observatories, Chinese Academy of Sciences, Beijing 100101, People's Republic of China
[8] Korea Astronomy and Space Science Institute, Daedeokdae-ro 776, Yuseong-gu, Daejeon 34055, Republic of Korea
[9] Roma Tre University, Rome 3169070, Italy
[10] Yale Center for Astronomy & Astrophysics and Department of Physics, Yale University, P.O. Box 208120, New Haven, CT 06520-8120, USA
[11] STAR Institute, Liège Université, Quartier Agora—Allée du six Août, 19c B-4000 Liège, Belgium
[12] Sterrenkundig Observatorium, Universiteit Gent, Krijgslaan 281 S9, B-9000 Gent, Belgium
[13] Scuola Normale Superiore, Piazza dei Cavalieri 7, I-56126 Pisa, Italy
[14] INAF—Osservatorio Astrofisico di Arcetri, Largo E. Fermi 5, I-50125 Firenze, Italy
[15] European Space Research and Technology Centre, Noordwijk-Binnen 2749812, The Netherlands
[16] Department of Astronomy, University of Maryland, College Park, MD 20742, USA
[17] Institute for Astronomy, 2680 Woodlawn Drive, University of Hawaii, Honolulu, HI 96822, USA

Received 2025 July 18; revised 2025 September 15; accepted 2025 September 19; published 2025 November 25

Abstract

Galaxy mergers are believed to play an important role in triggering rapid supermassive black hole (SMBH) growth. As merging nuclei approach each other, the physical properties of the participating galaxies and the associated SMBH growth are expected to evolve significantly. This study measures and characterizes these physical properties throughout the merger sequence. We constructed multiwavelength spectral energy distributions (SEDs) from hard X-rays to the far-IR for a sample of 72 nearby active galactic nucleus (AGN) host galaxies. The sample comprises 64 interacting systems, including single AGN in mergers and dual AGN, with nuclear separations $\leqslant$30 kpc, as well as eight isolated active galaxies with merging features. We carefully adapted available photometric measurements at each wavelength to account for their complex morphologies and varying spatial resolutions, to perform SED fitting using CIGALE, aimed to derive critical physical properties. Our results reveal that merging galaxies hosting AGN(s) show deviations from the star-forming main sequence and a wide range of star formation rates (SFRs). Both AGN activity and star formation are significantly influenced by the merger process, but these effects are more prominent in major (mass ratios $<$ 4:1) interactions. We find that the projected nuclear separation is not a good tracer of the merger stage. Instead, morphological classification accurately assesses the merger progression. Based on this morphological analysis, late-stage mergers exhibit elevated SFRs (5.1×), AGN luminosities (2.4×), and nuclear obscuration (2.8×) compared to earlier stages, supporting previous findings and reinforcing the link between merger-driven galaxy evolution and SMBH growth.

Unified Astronomy Thesaurus concepts: Galaxy mergers (608); Spectral energy distribution (2129); AGN host galaxies (2017)

Materials only available in the online version of record: figure sets, machine-readable table

1. Introduction

Understanding the formation and growth of supermassive black holes (SMBHs) across cosmic time remains among the most critical challenges in extragalactic astronomy. Observational evidence shows that the properties of galaxies strongly correlate with those of the SMBHs in their nuclei (J. Kormendy & D. Richstone 1995; J. Magorrian et al. 1998; L. Ferrarese & D. Merritt 2000; K. Gebhardt et al. 2000; K. Bandara et al. 2009; K. Gültekin et al. 2009), suggesting a fundamental link between galaxy evolution and SMBH growth. Active galactic nuclei (AGN) are found in galaxies where material is being accreted onto the central black hole at high rates (D. Lynden-Bell 1969). However, for this material to reach the vicinity of the black hole, it must lose about 99% of its angular momentum (P. F. Hopkins & E. Quataert 2011, and references therein). Simulations indicate that large-scale galaxy mergers of two or more galaxies provide an efficient mechanism for the gas to cease equilibrium and fall toward the SMBH, triggering the AGN (T. Di Matteo et al. 2005; P. F. Hopkins et al. 2006, 2008). Observationally, the AGN–merger connection is well established (S. L. Ellison et al. 2019; A. La Marca et al. 2024), and in particular these mergers seem to be responsible for the most luminous AGN (E. Treister et al. 2012) and quasars (D. B. Sanders et al. 1988; L. Fan et al. 2016; T. Díaz-Santos et al. 2018), implying that such collisions substantially accelerate the SMBH growth, although contradictory results were reported, where luminous AGN do not originate from major galaxy mergers (e.g., M. Mechtley et al. 2016) or even are not associated with merging systems (e.g., N. L. Zakamska et al. 2019). Studying and finding these objects is crucial because the processes occurring before the final coalescence of SMBHs remain largely unknown and could potentially represent a significant fraction, up to ∼60%, of the total SMBH growth (E. Treister et al. 2012; K. Schawinski et al. 2015).

In the final stages of the merging process, when both nuclei of the merging galaxies approach each other (at separations of approximately 10 kpc, although the exact division is rather arbitrary), these systems are more likely to host an AGN (e.g., M. Koss et al. 2010, 2011; S. L. Ellison et al. 2011; A. Stemo et al. 2021). This finding suggests that, at those close separations, the gas and dust are efficiently transported toward the galactic center, thereby fueling the SMBH growth. This is also seen in simulations (e.g., J. E. Barnes & L. E. Hernquist 1991; S. Byrne-Mamahit et al. 2024).

Observations have shown that merger-triggered AGN are likely to become heavily obscured by gas and dust (e.g., C. Ricci et al. 2017a, 2021; R. W. Pfeifle et al. 2019), particularly at later stages of the process. Additionally, galaxy merger simulations further predict that, along with this obscuration, a peak in SMBH accretion occurs when the two galactic nuclei are near each other prior to coalescence (e.g., L. Blecha et al. 2018). Due to the strong effect of obscuration, many AGN in merging galaxies remain undetected at optical to even soft X-ray (<10 keV) wavelengths. However, a sizable fraction can be found through hard X-ray observations, which are capable of penetrating dense gas and dust columns and are therefore less affected by obscuration (C. Ricci et al. 2015; T. T. Ananna et al. 2022). Notable surveys employing this approach include Swift/Burst Alert Telescope (BAT; K. Oh et al. 2018) and NuSTAR (F. A. Harrison et al. 2016).

The majority of AGN are found in isolated, nonmerging galaxies and are referred to as single AGN. However, AGN can also reside in merging systems. When only one nucleus hosts an AGN, the system is often referred to as a single AGN in a merger (single AGN iM), whereas when both nuclei are active, the system is defined as a dual AGN (e.g., J. M. Comerford et al. 2009; M. Koss et al. 2012). Observations have shown that the fraction of dual AGN increases as the merger progresses (e.g., M. Koss et al. 2012; H. Fu et al. 2018). However, it remains uncertain whether these phenomena represent different stages of the merger process (A. Bhattacharya et al. 2023) or both nuclei eventually become active at other times owing to the disparity in timescales between mergers and AGN activity ($t_{\rm AGN} \ll t_{\rm merger}$; S. Van Wassenhove et al. 2012), along with an intrinsic AGN variability that could change the accretion rate of the source from minutes to decades (e.g., M. Wold et al. 2007).

The triggering of AGN activity is not the only consequence of galaxy mergers. The accumulation of matter in the inner regions of galaxies during these events can also lead to elevated star formation rates (SFRs; e.g., V. Springel et al. 2005). It is well established that the formation of massive galaxies begins with an intense phase of star formation in the early epochs (SFR$_{\rm MS}$ at $z < 2$; e.g., B. Diemer et al. 2017). Over time, the available gas is gradually consumed, and the galaxy settles into a stabler star-forming phase, with SFRs typical of massive, star-forming galaxies defined as the main sequence (MS), which are generally classified as late-type galaxies (e.g., D. Elbaz et al. 2011). However, when these galaxies undergo a merger, the interaction can trigger a new starburst event in the nuclear region of the system ($>4 \times$ SFR$_{\rm MS}$; e.g., D. B. Sanders et al. 1988; G. Rodighiero et al. 2011; C. Schreiber et al. 2015; S. Yamada et al. 2023; A. M. M. Reeves & M. J. Hudson 2024), significantly enhancing the SFR in both progenitor galaxies (e.g., G. Jin et al. 2021). Eventually, the merger-driven starburst exhausts the cold gas reservoir and quenches star formation, producing a massive, passive remnant. These systems, known as early-type galaxies, are now understood to be the final outcome of the merger process and its associated evolutionary phases (e.g., S. Veilleux et al. 2002; V. Springel et al. 2005; K. Schawinski et al. 2014).

Many previous studies have investigated merging galaxies using imaging techniques (e.g., D. B. Sanders et al. 1988; S. L. Ellison et al. 2008, 2011; J. M. Scudder et al. 2012; G. Jin et al. 2021) and simulations (e.g., J. C. Mihos & L. Hernquist 1996; P. Di Matteo et al. 2008; P. F. Hopkins et al. 2008; S. Byrne-Mamahit et al. 2024). However, these studies have not focused on the sources with the closest separations, particularly in those hosting an active nucleus (or two). Detecting mid- and late-stage mergers hosting AGN requires high spatial resolution data to resolve closely separated nuclei, making angular resolution crucial for such studies. Additionally, as previously noted, nuclear obscuration plays a key role in identifying these systems. Therefore, observations at wavelengths less affected by dust obscuration, such as the mid-IR (MIR) or X-ray bands, are also essential. A summary of all AGN hosted by galaxies involved in mergers and how they were identified is presented in R. W. Pfeifle et al. (2025).

Measuring the physical properties of such sources is challenging owing to the vast spectral range typically covered by the AGN emission, spanning from X-rays originating in the corona, to UV/optical from the accretion disk, to IR from the dusty torus, to millimeter emission also partly from the corona. This wide wavelength coverage creates a highly degenerate problem to characterize the AGN emission and separate it from the host galaxy, particularly when data coverage and depth are limited. To address this, assembling multiband photometric data and fitting spectral energy distributions (SEDs) offers a robust approach to disentangling the different emission components of a galaxy and accurately determining its physical properties. This method has been employed in various studies for AGN sources (e.g., R. A. Edelson & M. A. Malkan 1986; M. Polletta et al. 2007; G. Yang et al. 2022).

Merging galaxies are expected to exhibit distinct physical properties compared to nonmerging systems (e.g., S. L. Ellison et al. 2008). These properties are believed to evolve throughout the merger process, with particularly strong changes observed at projected separations below 30 kpc, such as AGN activity (e.g., S. L. Ellison et al. 2011), AGN obscuration (e.g., S. Satyapal et al. 2014), and elevated SFRs (e.g., D. R. Patton et al. 2013). Therefore, studying merging systems at these separations provides crucial insights into how the interaction during merger stages shapes the nuclear activity, as well as the resulting physical characteristics of the galaxies involved (J. M. Scudder et al. 2012).

In this paper, we investigate how galaxy mergers impact the physical properties of SMBHs and their host galaxies across different stages of the merger process. To achieve this, we analyze a sample of merging systems with projected nuclear separations spanning up to 30 kpc, using multiband SED fitting with wavelength coverage from hard X-rays to the far-IR (FIR). Section 2 describes the sample selection process. In Section 3, we present the wavelength bands used and explain how photometric fluxes are measured for SED fitting. The detailed procedure for fitting SEDs using the Code Investigating GALaxy Emission (CIGALE; M. Boquien et al. 2019) is outlined in Section 4. The derived physical parameters are presented and analyzed in Section 5, providing insight into the effects of mergers on SMBHs and their host galaxies. Finally, a discussion of the results and our conclusions are presented in Sections 6 and 7, respectively. Throughout this paper, we assume a flat ΛCDM cosmology with $H_0 = 70\,\mathrm{km\,s^{-1}\,Mpc^{-1}}$, $\Omega_m = 0.3$, and $\Omega_\Lambda = 0.7$.

2. Sample

The sources analyzed in this work were selected from the BAT AGN Spectroscopic Survey[18] (BASS; M. J. Koss et al. 2022b), which comprises the most luminous hard-X-ray-selected AGN in the local Universe. From this parent sample, we selected a subset of merging systems with small radial velocity differences ($<300\,\mathrm{km\,s^{-1}}$; M. Koss et al. 2012) in the nearby Universe ($z < 0.1$), where the relatively small distances allow us to spatially resolve the nuclei of the participating galaxies to small physical separations.

To identify these systems, we use three complementary approaches. First, we selected candidates for late-stage mergers that might have projected nuclear separations of less than 10 kpc. These sources were required to exhibit merging features (e.g., disturbed disks and/or tidal tails) and/or have a close companion. To better resolve these systems, they were observed with the Gemini South Adaptive Optics Imager (GSAOI; P. McGregor et al. 2004), a near-IR adaptive optics instrument installed on the Gemini Multi-Conjugate Adaptive Optics System at Gemini South in northern Chile. GSAOI has a pixel size of $0\farcs02\,\mathrm{pixel^{-1}}$ and consists of four 2048 × 2048 chips with $2''$ gaps, providing a field of view of $85'' \times 85''$. Using GSAOI, 22 sources were observed in the H (1.64 μm) and K_s (2.16 μm) bands between 2021 December and 2022 December (GS-2021B-Q-132, GS-2022A-Q-140, GS-2022B-Q-234). These images were reduced with THELI v3 (M. Schirmer 2013). This data set enabled us to measure the projected separation of the merging systems or assess whether the sources were involved in mergers. We identified 4 sources with separations below 10 kpc, 10 mergers with larger separations, and 8 sources not involved in mergers but exhibiting merger features.

The second selection comes from the sample of BASS AGN studied by M. J. Koss et al. (2018), who reported the identification of 17 late-stage mergers. This subsample includes mergers with separations ranging from 0.3 to 10 kpc.

The third selection is based on a sample of mergers with already-measured separations between 4 and 28 kpc, thereby expanding the range of separations studied in this work. These galaxies were selected from the merger sample identified by M. Koss et al. (2012) using the 70-month BAT catalog (W. H. Baumgartner et al. 2013), later expanded to include the southern hemisphere and the 105-month sample (K. Oh et al. 2018). These objects were also observed in the millimeter with the Atacama Compact Array (ACA; S. Iguchi et al. 2009) under project ID 2023.1.01471.S. This subsample contributes 33 sources to the final sample.

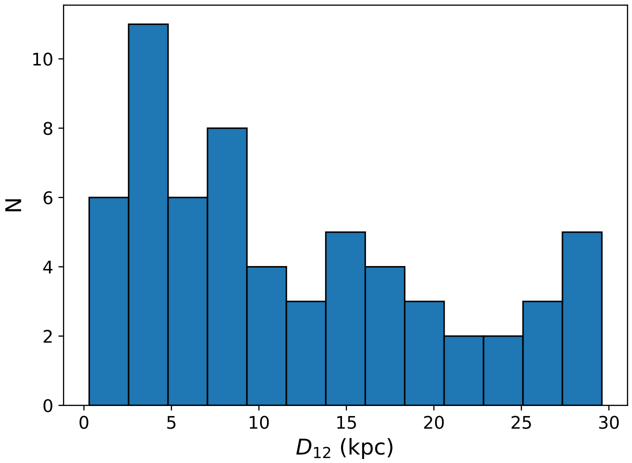

Figure 1. Distribution of projected nuclear separation in kpc, for the 64 galaxies involved in merging systems in our sample; 35/64 galaxies are late-stage mergers ($D_{12} < 10$ kpc).

The parameters used to measure the projected nuclear separations in kpc are the redshift and projected separation in arcsec. (1) The redshifts used in this work were primarily measured from the [O III] emission line in the Narrow-Line Region (M. J. Koss et al. 2022a). For the BASS sample, this line has, in general, a very high signal-to-noise ratio (S/N). The spectra were obtained with resolutions of $R \approx 1200$–6000 using Palomar/DBSP and Very Large Telescope/X-shooter, corresponding to velocity uncertainties of only 20–50 $\mathrm{km\,s^{-1}}$. In redshift space, at $z \approx 0.03$, this translates to an associated uncertainty of ∼0.3%. Such small uncertainties have a negligible impact on the projected separations. (2) Projected separations (in arcsec) are determined from the centroids of the galaxies. The main source of uncertainty is therefore how accurately the centroids can be measured, which is limited by the angular resolution of the imaging and improves with increasing S/N, which for the nuclear regions is usually high. For the GSAOI sample, where the separations were measured directly in this work, the angular resolution is $\sim0\farcs1$, yielding well-resolved centroids with negligible positional uncertainties. For the M. J. Koss et al. (2018) late-stage merger sample ($D_{12} < 10$ kpc), which relies on Keck adaptive optics (AO) imaging (resolution $\sim0\farcs17$), the situation is similar. For the larger merger sample, in the worst case images from the Dark Energy Survey (DES), the Sloan Digital Sky Survey (SDSS), or LEGACY (resolution $\sim1\farcs0$) were used for this measurement, but even in these cases the projected separations are mostly above $10''$, so the relative uncertainty remains negligible.

In total, our data set includes 72 sources, which are summarized in Table 1. Of these, 64 are merging systems spanning projected separations ranging from 0.3 to 29.6 kpc. Figure 1 shows the projected separation distribution in the merging sample, defined as the distance between the two nuclei projected onto the plane of the sky, measured in kpc.

---

[18] https://www.bass-survey.com

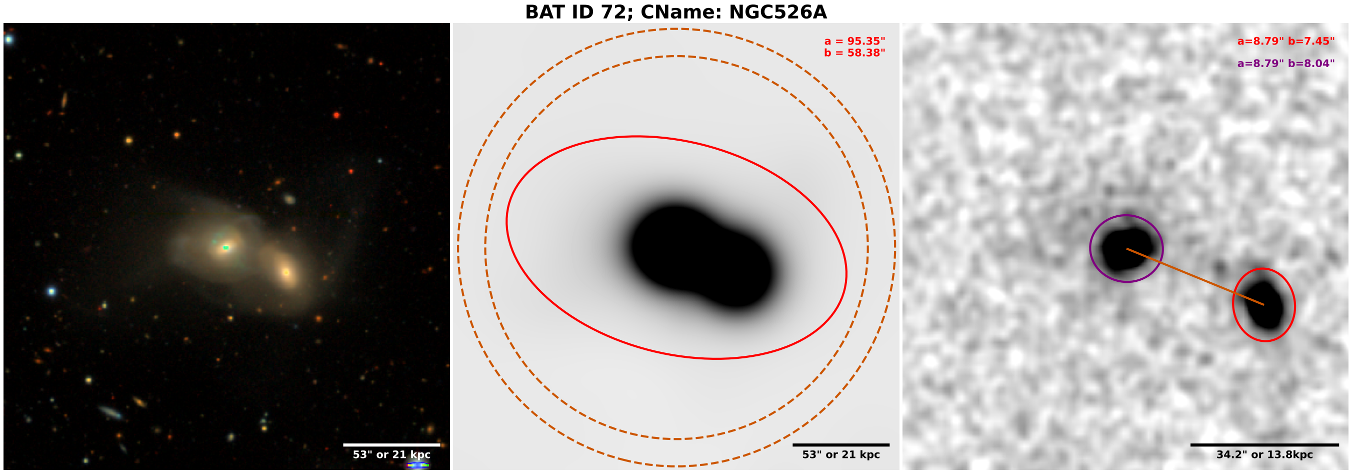

Figure 2. Left: Red, green, and blue image for BAT ID: 72 constructed from the g, r, and z filters. Middle: example convolved image presenting the aperture and annulus used for the photometry. Right: NIR image from 2MASS in the K_s band, showing the apertures for the M_1/M_2 measurement and the projected separation indicated by the scale bar.

(The complete figure set (71 images) is available in the online article.)

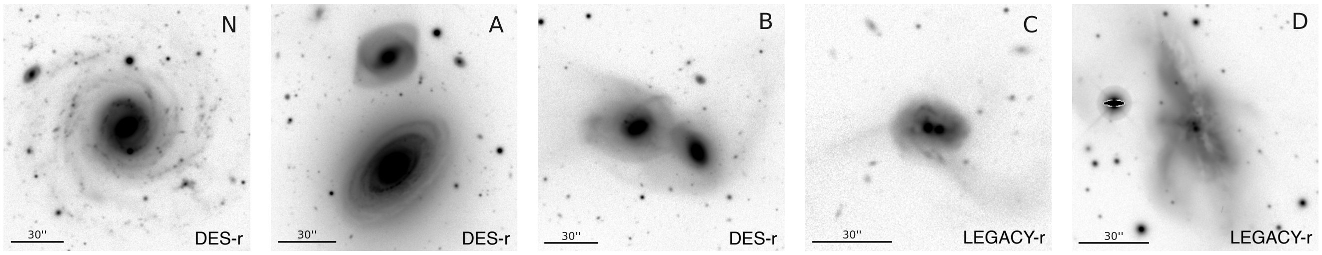

Figure 3. From left to right: N—nonmerging/isolated galaxies; A—pre-stage merger; B—early-stage merger; C—mid-stage merger; D—late-stage merger.

Among them, nine sources are confirmed dual AGN based on millimeter and/or X-ray observations (M. Koss et al. 2012), and 55 are classified as single AGN in mergers, where only one AGN is identified.

We estimated stellar mass ratios (M_1/M_2) using NIR fluxes as a proxy. In particular, we use the K filter for these measurements: the Two Micron All Sky Survey (2MASS) for separated sources, and GSAOI and Keck for closer companions. In some particular cases, we used the Hubble Space Telescope (HST) F160W filter and the VISTA Hemisphere Survey K band. All images used are presented in Figure 2.

For the systems in our sample, we adopted a 4:1 mass ratio as the dividing boundary between major and minor mergers (e.g., A. Toomre & J. Toomre 1972; H. M. Hernández-Toledo et al. 2005; C. J. Conselice 2006). Based on this criterion, 33 systems can be classified as major mergers and 31 as minor mergers. Additionally, eight galaxies from the GSAOI sample exhibit merger features without a visible companion, suggesting that they may be in an advanced merger stage, may have already coalesced, or may not be involved in mergers. Figure 2 presents an example, and the full subset of sources is illustrated in Figure Set 2.

2.1. Optical Morphologies

We visually classify our sources based on their optical morphology, using r-band images from the available surveys for each object (e.g., DES, SDSS, DECaLS, Pan-STARRS, etc.). To asses the merger stage, we examine characteristic merger features (such as tidal tails and/or disturbed disks) and the projected separation between the two nuclei, following the classification scheme of S. Stierwalt et al. (2013). The first stage, known as the pre-stage merger (A), occurs when two galaxies begin to interact and move closer to one another, without physical contact. In the early-stage merger (B), both galaxies have had their first encounter but still maintain symmetric disks, with only faint tidal features. The system evolves into a mid-stage merger (C), characterized by amorphous disks and the most pronounced merger features, as the interaction continues. Finally, in the late-stage merger (D), both nuclei merge into a single envelope, just before coalescence. Additionally, there is a category for nonmerging systems (N), in which we include sources that do not show evidence of two distinct nuclei. Morphological data alone do not allow us to determine whether these cases correspond to isolated nonmerging systems (i.e., N comes before A) or post-merger systems (i.e., N comes after D). Likely, this bin includes a mix of them. Figure 3 presents an example of a system in each stage. While human-based morphological classification is inherently subjective, any ambiguities in assigning merger stages, aside from the N category, will not affect the overall trends and general conclusions presented in this study.

2.2. Control Sample

To compare our merging sample with noninteracting galaxies, we select 532 nonactive galaxies from xCOLD GASS with the measurements of SFR and stellar mass (M_*) from A. Saintonge et al. (2017). These galaxies lie in the redshift range $0.01 < z < 0.05$, with SFRs between $0.02 < \mathrm{SFR}/M_\odot\ \mathrm{yr}^{-1} < 34.5$ and stellar masses $M_* > 10^9\ M_\odot$.

Table 1
Sample of AGN-hosting Galaxy Mergers Used in This Work

ID	SWIFT	Object Name	z	D_{12} (arcsec)	D_{12} (kpc)	M1/M2	AGN Type	Merger AGN	Stage
Major Galaxy Mergers									
405	J0804.6+1045	UGC 4211	0.035	0.3	0.3	3.6	Sy2	dual AGN	D
841	J1652.9+0223	NGC 6240	0.025	1.8	0.9	2.1	Sy2	dual AGN	D
13	J0025.8+6818	LEDA 136991	0.012	4.3	1.1	1.3	Sy2	single AGN iM	C
998	J1845.4+7211	Z341-6	0.047	1.3	1.2	1.7	Sy2	dual AGN	D
88	J0138.8+2925	LEDA 138434	0.072	1.2	1.8	2.8	Sy1.9	single AGN iM	D
60	J0113.8+1313	Mrk 975	0.05	2.5	2.5	2.3	Sy1	single AGN iM	C
243	J0450.7–5813	RBS 594	0.09	1.5	2.6	3.9	Sy1	single AGN iM	D
817	J1631.7+2353	SDSS J163115.52+235257.4	0.059	2.3	2.7	2.1	Sy1.9	dual AGN	C
552	J1136.0+2132	Mrk 739E	0.029	6.1	3.7	1.3	Sy1	dual AGN	C
533	J1114.3+2020	2MASX J11140245+2023140	0.027	7.6	4.1	2.8	Sy2	single AGN iM	D
641	J1252.3–1323	NGC 4748	0.014	15.7	4.7	3.9	Sy1	single AGN iM	C
157	J0255.2–0011	NGC 1142	0.029	8.5	4.8	2.5	Sy2	single AGN iM	C
703	J1355.9+1822	Mrk 463	0.05	4.8	4.9	3.6	Sy1.9	dual AGN	C
1139	J2207.3+1013	UGC 11910	0.027	14.3	7.9	2.3	Sy2	single AGN iM	C
678	J1334.8–2328	ESO 509-IG066	0.034	12.1	8.1	2.5	Sy1.9	single AGN iM	B
497	J1023.5+1952	NGC 3227	0.003	153.0	8.9	1.8	Sy1	dual AGN	B
605	J1214.3+2933	Was49b	0.063	7.1	9.2	1.9	Sy1	single AGN iM	C
862	J1708.6+2155	SDSS J170859.13+215308.1	0.073	6.7	10.0	3.3	Sy1	dual AGN	B
260	J0508.1+1727	2MASX J05081967+1721483	0.017	29.4	10.6	2.8	Sy1.9	single AGN iM	A
72	J0123.8–3504	NGC 526A	0.019	35.9	13.8	2.0	Sy1.9	dual AGN	B
1356	J0941.2–3846	2MASX J09410102–3847509	0.064	11.9	14.9	2.7	Sy2	single AGN iM	A
567	J1145.6–1819	HE 1143–1810	0.033	22.2	14.9	2.9	Sy1	single AGN iM	B
1141	J2209.1–2747	NGC 7214	0.023	33.9	15.6	4.0	Sy1	single AGN iM	C
1262	J0324.9–0304	NGC 1320	0.008	95.1	15.6	1.7	Sy2	single AGN iM	A
44	J0100.9–4750	2MASX J01003490–4752033	0.048	18.7	17.7	2.7	Sy2	single AGN iM	B
280	J0528.1–3933	LEDA 17320	0.037	23.0	18.1	1.7	Sy1	single AGN iM	B
231	J0440.2–5941	LEDA 15768	0.058	16.2	18.2	3.2	Sy2	single AGN iM	B
1627	J2328.1+0883	NGC 7674	0.028	33.4	18.8	4.0	Sy2	single AGN iM	C
343	J0640.0–4737	SWIFT J064013.50–474132.9	0.057	20.3	22.8	1.9	Sy2	single AGN iM	N
1077	J2028.5+2543	NGC 6921	0.014	91.0	26.2	3.1	Sy2	single AGN iM	A
1077	J2028.5+2543	MCG +04-48-002	0.013	91.0	26.2	3.2	Sy2	single AGN iM	A
712	J1413.2–0312	NGC 5506	0.006	223.8	28.3	2.0	Sy1.9	single AGN iM	A
606	J1217.2–2611	ESO 505-30	0.04	37.7	29.6	2.2	Sy2	single AGN iM	B
Minor Galaxy Mergers									
318	J0606.0–2755	2MASX J06054896–2754398	0.09	1.7	2.9	9.0	Sy1	single AGN iM	D
430	J0843.5+3551	CASG 218	0.054	2.7	2.9	9.1	Sy2	single AGN iM	D
134	J0234.6–0848	NGC 985	0.043	3.8	3.4	6.9	Sy1	single AGN iM	D
189	J0342.0–2115	ESO 548-81	0.014	13.4	3.8	8.8	Sy1	single AGN iM	C
305	J0548.4–4748	LEDA 17883	0.05	4.6	4.5	4.8	Sy2	single AGN iM	D
543	J1126.7+3514	Mrk 423	0.032	9.1	6.0	4.8	Sy2	single AGN iM	C
557	J1139.0–2323	HE 1136–2304	0.027	11.8	6.4	36.5	Sy1.9	single AGN iM	B
669	J1321.2+0859	LEDA 46599	0.033	25.0	6.6	13.8	Sy1.9	single AGN iM	C
303	J0544.4+5909	2MASX J05442257+5907361	0.068	4.8	6.6	7.6	Sy1.9	single AGN iM	C
63	J0114.4–5522	NGC 454E	0.012	27.8	6.9	11.2	Sy2	single AGN iM	C
1130	J2156.2+1724	2MASX J21561518+1722525	0.034	10.9	7.3	5.3	Sy1	single AGN iM	A
1439	J1416.5–3671	PKS 1413–36	0.074	5.6	8.6	7.8	Sy2	single AGN iM	B
28	J0042.9–2332	NGC 235A	0.022	19.6	8.9	5.3	Sy1.9	single AGN iM	B
159	J0256.4–3212	ESO 417-6	0.017	28.0	9.2	82.7	Sy2	single AGN iM	B
218	J0423.5+0414	LEDA 15023	0.046	10.2	9.3	29.3	Sy2	single AGN iM	B
89	J0140.6–5321	2MASX J01402676–5319389	0.072	6.8	9.5	24.1	Sy1.9	single AGN iM	B
1063	J2007.0–3433	CTS 28	0.025	18.8	9.5	14.0	Sy1	single AGN iM	C
302	J0544.4–4328	2MASX J05440009–4325265	0.044	15.1	13.1	6.6	Sy2	single AGN iM	B
136	J0238.2–5213	ESO 198-24	0.045	15.1	13.5	20.8	Sy1	single AGN iM	B
217	J0422.7–5611	Fairall 302	0.044	18.0	15.5	4.4	Sy2	single AGN iM	A
465	J0934.7–2156	ESO 565-19	0.016	52.2	17.6	8.7	Sy2	single AGN iM	A
329	J0623.9–6058	ESO 121-28	0.04	24.1	19.1	7.3	Sy2	single AGN iM	B
316	J0602.2+2829	IRAS 05589+2828	0.033	28.3	19.2	9.7	Sy1	single AGN iM	A
193	J0350.1–5019	ESO 201-4	0.036	27.4	20.6	4.6	Sy2	single AGN iM	B
416	J0823.4–0457	Fairall 272	0.022	44.8	20.6	877.7	Sy2	single AGN iM	B

Table 1
(Continued)

ID	SWIFT	Object Name	z	D_{12} (arcsec)	D_{12} (kpc)	M1/M2	AGN Type	Merger AGN	Stage
1255	J0306.0–3902	NGC 1217	0.021	57.3	24.4	11.6	LINER	single AGN iM	A
73	J0123.9–5846	Fairall9	0.046	27.3	24.6	14.6	Sy1	single AGN iM	B
1182	J2303.3+0852	NGC 7469	0.016	78.6	26.0	6.2	Sy1	single AGN iM	A
471	J0945.6–1420	NGC 2992	0.008	175.8	27.6	5.6	Sy1.9	single AGN iM	B
246	J0454.6–4315	LEDA 146662	0.087	16.8	28.5	10.0	Sy1.9	single AGN iM	A
197	J0354.2+0250	HE 0351+0240	0.036	13.1	29.6	36.2	Sy1	single AGN iM	B
Single Galaxies									
342	J0640.4–2554	ESO 490-26	0.025	S	S	S	Sy1	single AGN	D
584	J1200.2–5350	LEDA 38038	0.028	S	S	S	Sy2	single AGN	N
1210	J2359.3–6058	PKS 2356–61	0.096	S	S	S	Sy2	single AGN	N
489	J1009.3–4250	ESO 263-13	0.034	S	S	S	Sy2	single AGN	N
1390	J1127.6–2912	ESO 439-G009	0.023	S	S	S	Sy2	single AGN	N
1426	J1334.1–3842	WISEA J133359.07–382450.3	0.052	S	S	S	Unknown	single AGN	N
83	J0131.8–3307	ESO 353-9	0.016	S	S	S	Sy2	single AGN	N
442	J0902.8–7414	2MASX J09034285–7414170	0.091	S	S	S	Sy2	single AGN	N

Note. The table is divided according to stellar mass ratio (M_1/M_2) using $M_1/M_2 = 4$ as the separation between major and minor galaxy mergers. Each subset is sorted by projected separation (D_{12} kpc). Column (1): target BAT ID. Column (2): SWIFT name. Column (3): counterpart name. Column (4): redshift measured from BASS. Columns (5)–(6): projected separation between the two nuclei in arcseconds and kpc. "S" mean that the source does not have a companion. Column (7): mass ratio between primary and secondary galaxy based on NIR emission. Column (8): AGN type based on optical spectroscopy (M. J. Koss et al. 2022a). Column (9): type of merging AGN, as explained in Section 1. Column (10): merger stage, as explained in Section 2.1.

(This table is available in machine-readable form in the online article.)

Moreover, we include 213 local AGN-host galaxies ($0.01 < z < 0.05$) from the BASS sample with available measurements of SFR ($0.02 < \mathrm{SFR}/M_\odot\,\mathrm{yr}^{-1} < 132$) and stellar mass ($10^{9.5} < M_*/M_\odot < 10^{11.5}$), provided by M. J. Koss et al. (2021), who also compare these AGN hosts directly with the xCOLD GASS galaxies. Furthermore, these sources have measurements of AGN bolometric luminosities ($10^{43} < L_{\mathrm{bol}}/\mathrm{erg\,s}^{-1} < 10^{46}$), as reported by C. Ricci et al. (2017b).

3. Photometry

We use all available photometric bands from the X-ray to the FIR to cover a wide wavelength range for SED fitting. To ensure accurate relative photometric calibrations, we developed a set of custom procedures in Python, described in Section 3.1, to match the apertures and resolutions of the sources in the different photometric bands, in order to minimize wavelength-dependent differences in the fraction of the integrated emission, addressing inconsistencies in aperture sizes and measurement methods in the available UV-to-FIR survey data, which can significantly impact SED fitting. This is done by incorporating images from different surveys. At X-ray wavelengths, we use the intrinsic fluxes obtained from C. Ricci et al. (2017b), as will be presented in Section 3.4. To complete our photometric study, we incorporate measurements from the following surveys:

1. *UV*. Data were obtained from the Galaxy Evolution Explorer (GALEX; D. C. Martin et al. 2005) in its far-UV (153 μm) and near-UV (229 μm) bands (spatial resolutions of $4\overset{''}{.}5$ and $6\overset{''}{.}0$, respectively).
2. *Optical*. We use optical data from three surveys to ensure coverage for all our sources in the entire sky: (1) DES (T. M. C. Abbott et al. 2018) in the *grizY* filters (0.48, 0.62, 0.75, 0.87, and 1.02 μm; spatial resolution from $0\overset{''}{.}9$ to $1\overset{''}{.}2$), (2) Sloan Digital Sky Survey (SDSS; D. G. York et al. 2000) in the *ugriz* filters (0.36, 0.47, 0.62, 0.75, and 0.89 μm; spatial resolutions ranging from $1\overset{''}{.}3$ to $2\overset{''}{.}0$), and (3) the DECam Legacy Survey (DECaLS; A. Dey et al. 2019) in the *griz* filters (0.48, 0.62, 0.75, and 0.87 μm; spatial resolutions from $1\overset{''}{.}0$ to $1\overset{''}{.}2$).
3. *NIR*. For the near-IR emission, we use 2MASS (M. F. Skrutskie et al. 2006) in the J (1.25 μm), H (1.65 μm), and K_s (2.17 μm) filters (spatial resolutions from $2\overset{''}{.}0$ to $2\overset{''}{.}5$).
4. *MIR*. MIR data are taken from the Wide-field Infrared Survey Explorer (WISE; E. L. Wright et al. 2010) using the AllWISE data release, in its W1(3.4 μm), W2 (4.6 μm), W3 (12 μm), and W4 (22 μm) bands (spatial resolution from $6\overset{''}{.}1$ to $12\overset{''}{.}0$).
5. *FIR*. For FIR emission, we use the Photodetector Array Camera and Spectrometer (PACS; A. Poglitsch et al. 2010) on board Herschel in its 70 and 160 μm bands (spatial resolutions of $5\overset{''}{.}8$ and $12\overset{''}{.}0$, respectively).

Not all sources have available data in all bands. Table 2 summarizes the information about the availability of bands for each source. One source, BAT ID 343, was excluded from the final sample because its fluxes could not be measured owing to the presence of a bright nearby star, which affected the measurements and prevented CIGALE from obtaining a reliable fit. As a result, the final sample consists of 71 sources.

3.1. Flux Measurements

By selection, the sources in our sample exhibit complex and disturbed morphologies, making it challenging to obtain consistent apertures and resolutions across different surveys.

Table 2
Available Multiwavelength Photometry Used on the SED Fitting

X-Rays	UV	Optical	NIR	MIR	FIR	No. Sources
✓	✓	✓	✓	✓	✓	25
✓	✓	✓	✓	✓	x	19
✓	✓	x	✓	✓	✓	4
✓	x	✓	✓	✓	✓	1
x	✓	✓	✓	✓	✓	1
✓	✓	✓	x	✓	✓	1
✓	✓	x	✓	✓	x	2
✓	x	✓	✓	✓	x	5
✓	x	x	✓	✓	✓	3
x	✓	✓	✓	✓	x	5
✓	x	x	✓	✓	x	1
x	✓	x	✓	✓	x	2
x	x	x	✓	✓	✓	2
Total						71

To address this, we follow the procedure developed by A. Rojas et al. (2025, in preparation) to get reliable photometric measurements while minimizing contamination from nearby objects and ensuring that the bands' apertures and spatial resolutions are matched. In the following, we outline the steps in our methodology:

1. *Identifying target galaxies and surrounding sources*. To identify well-detected sources, we first apply a 2σ threshold above the background to identify significant emission. Then, using the system coordinates, we locate the source of interest. If, at this threshold, we do not identify low-brightness features, which are essential for the photometry, we manually define a precise region using DS9 for each band. This region is also helpful for excluding unrelated nearby sources that are not part of the galaxy. This step ensures that the primary galaxy is accurately identified while minimizing contamination from adjacent sources. If the merging system is resolved in the lowest-resolution band (W4), we target only the BASS source (7/72). However, if it remains unresolved in W4, we include both the BASS source and its counterpart to ensure consistency across all wavelengths (65/72).
2. *Removal/replacement of surrounding sources*. Once surrounding sources are identified (either automatically or manually via DS9 regions), they are removed by replacing their pixel values using random background values, from the entire field, to simulate an image containing only the target surrounded by background noise. If a foreground star overlaps with the galaxy, it is identified using the Gaia DR3 (Gaia Collaboration et al. 2023) catalog and subsequently removed while extrapolating the galaxy's brightness profile in the region occupied by the star. This procedure introduces a small increase in the local deviation within the replaced region compared to the rest of the image, particularly in similar regions. However, this effect is smoothed out in the subsequent processing steps.
3. *Resolution matching*. To ensure consistent resolution across all the bands, we convolve all images to achieve a final angular resolution of $\sim 12''$, which matches the resolution of the WISE W4 band. This step is critical for minimizing systematic biases introduced by differences in the spatial resolution of the data.
4. *Flux measurements*. Finally, after the convolution, fluxes are measured using a single aperture across all bands. Each source's aperture size is individually chosen based on the morphology and inclination, ensuring that it is large enough to encompass the whole galaxy and captures all of its flux in all the available bands, while remaining as small as possible. To achieve this, we adopt a human-guided aperture selection method, using flux–aperture plots to verify that the chosen aperture includes the galaxy's total emission. In addition, an annular region is used to estimate the local background. This uniform approach enables consistent and reliable measurements across the entire spectral range.

Figure 4 presents a graphical representation and an example of the photometric method followed here.

3.2. Photometric Errors

To estimate the photometric uncertainties, we consider two main sources of random noise: Poisson fluctuations from the source signal, and background noise from the surrounding sky.

The Poisson noise is estimated from the square root of the source counts, while the background noise is measured from the standard deviation of the background values in an annular region around the source. These components are combined and scaled by a conversion factor (k), which transforms counts (or instrumental units) into physical flux units (mJy). The total uncertainty is then computed as

$$\sigma_{\mathrm{mJy}} = k\sqrt{(\sqrt{\mathrm{counts}})^2 + \sigma_{\mathrm{bkg}}^2}. \tag{1}$$

For surveys where the detector gain is available, such as 2MASS and DES, we use the `calc_total_error`[19] function from the `photutils` package. This method provides a more accurate estimate of the total error by properly incorporating gain information, read noise, and background variance.

3.3. Foreground Galactic Extinction Correction

The fluxes from the FUV to W2 bands were corrected for galactic extinction to account for the Milky Way reddening. For this, we utilized the Python library `dustmaps` (G. Green 2018), which enabled us to determine the reddening value $E(B-V)_{\mathrm{SFD}}$ for each source. The individual extinction values were then calculated using the following relation:

$$A_\lambda = R_\lambda E(B-V)_{\mathrm{SFD}}, \tag{2}$$

where R_λ is the extinction coefficient for each band. These values were obtained from E. F. Schlafly & D. P. Finkbeiner (2011) for SDSS, DES, and DECaLS and from H. B. Yuan et al. (2013) for GALEX, 2MASS, and WISE. This correction was negligible for bands redder than W2 and hence was not applied in those cases.

---

[19] https://photutils.readthedocs.io/en/stable/api/photutils.utils.calc_total_error.html

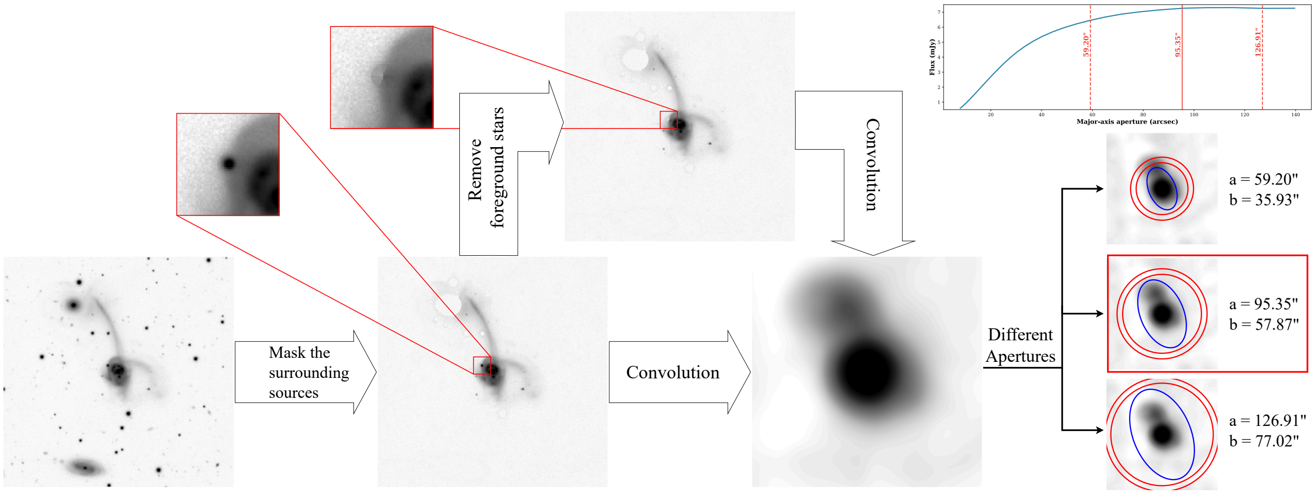

Figure 4. Schematic visualization of the custom-made code developed for flux measurements. The first panel shows the stacked image downloaded from the relevant survey (in this case, as an example, we show the source BAT ID 305 in the DES-*r* band). The second step removes the surrounding sources, replacing their pixels with random values obtained from the background. In the third step, if a foreground star lies along the line of sight, it is removed by extrapolating the galaxy's brightness profile across the region occupied by the star. If no foreground star is present, this step is skipped. In the fourth panel, we convolve the image to reduce its resolution to match the resolution of the WISE W4 band, which has the lowest. Finally, multiple apertures are applied to determine the optimal one for consistent measurements across all available bands (blue ellipses with "a" and "b" the ellipse axes). A circular annulus is also used to estimate the local background (red circles). The optimal aperture is selected as the smallest that fully encompasses the entire galaxy, guided by the flux–aperture plot. In this example, the chosen aperture is indicated by a red rectangle and the solid red line in the flux–aperture plot.

3.4. X-Ray Fluxes

Our photometric measurements were essential for recovering the total emission from each source. In contrast, X-ray emission originates from compact regions in the nucleus of a galaxy, making flux losses negligible. Therefore, we can directly use previous measurements of the X-ray fluxes. All galaxies in our study belong to the Swift/BAT sample and hence have hard X-ray measurements available in the literature. Specifically, we use the intrinsic (i.e., obscuration-corrected) X-ray fluxes reported by C. Ricci et al. (2017b) for the 2–10 keV and 14–195 keV bands. These fluxes were derived through spectral analysis using data from XMM-Newton, Swift/XRT, ASCA, Chandra, and Suzaku for soft X-rays and from Swift/BAT for hard X-rays. The resulting parameters include estimates of column densities ($N_{\rm H}$) and measurements of the photon index (Γ), which are then given to CIGALE as input values.

As a caveat, we remark that there is, on average, a spread of up to ∼10 yr between the X-ray observations and the remaining multiwavelength data sets (with 2MASS near-IR photometry showing the largest offsets). Consequently, some of the sources in our study could be affected by AGN variability. Nevertheless, since Swift/BAT fluxes are averaged over the years, short-term X-ray variability is significantly smoothed out.

4. SED Modeling

To constrain the physical properties of our sample, we employed CIGALE (M. Boquien et al. 2019) to perform SED fitting for each source. The fitting utilizes the photometry obtained in Section 3, which spans the UV-to-FIR range, and the X-ray fluxes from Section 3.4.

The host galaxy component was modeled using a delayed star formation history with an additional burst episode, as we expect galaxy mergers to undergo a starburst event. The stellar emission was represented by a single stellar population, as modeled by G. Bruzual & S. Charlot (2003). For dust attenuation, we adopted a modified version of D. Calzetti et al. (2000). Dust emission was modeled using the templates from B. T. Draine et al. (2014). The AGN emission was characterized using the SKIRTOR templates (M. Stalevski 2012), which account for the clumpy structure of the AGN torus. In particular, we modeled two AGN components using a modified version of CIGALE for the confirmed dual AGN in our sample. The two components differ primarily in the AGN fraction parameter: in the first AGN component, this fraction represents the ratio of the AGN IR emission to the total IR emission from the merging system, whereas for the second component it represents the contribution of the second AGN instead of the first. Finally, CIGALE utilizes a specific module, as described by G. Yang et al. (2020), to model the X-ray emission. As mentioned in Section 3.4, the photon index was provided as input to CIGALE, ensuring that the information from the hard X-ray band was incorporated. The parameter space and corresponding input values used for the SED fitting are summarized in Table 3.

To manage the increased complexity introduced by modeling two AGN components, we adopted a two-step fitting approach. In the first step, we fit our 71 sources using a single AGN component to constrain all parameters, generating approximately 7.46×10^9 models. In the second step, we reran the code for the confirmed nine dual AGN, now fixing the galaxy parameters obtained in the first step while allowing the two AGN components to vary independently, generating approximately 3.6×10^5 models. This strategy significantly reduces computational time, enabling a more accurate characterization of individual AGN parameters. The impact of using one or two AGN components is discussed in Section 6.3.1.

After running the fitting procedure, source BAT ID 497 failed to converge to a good solution and was therefore excluded from the final sample, resulting in 70 sources with available measured parameters.

To ensure the reliability of our parameter estimations, we utilized the mock analysis tool provided in CIGALE to validate our results. This tool generates synthetic observations based on the best-fit models and compares them to the input

Table 3
CIGALE Input Parameters, Generating 7.46×10^9 Models

Model	Module	Parameter	Value
SFH model	`sfhdelayedbq`	`tau_main`	1000, 3000, 5000
		`age_main`	4500, 7000, 9500, 12000
		`age_bq`	10, 20, 100
		`r_sfr`	0.1, 1, 10, 1000
Stellar emission	`bco3`	`imf`	1
Attenuation law	`dustatt_modified_starburst`	`E_BV_lines`	0.1, 0.5, 1.0, 1.5, 2.0
		`powerlaw_slope`	−0.8, −0.4, 0.0
Dust emission	`dl2014`	`qpah`	0.47, 1.12, 2.50
		`umin`	1, 5, 10, 25, 50
		`alpha`	2.0, 2.5
AGN	`skirtor2016`	`oa`	20, 40, 60, 80
		`i`	0, 30, 60, 90
		`fracAGN`	0.1, 0.2, 0.3, 0.4, 0.5, 0.6, 0.7, 0.8, 0.9
		`EBV`	0.0, 0.05, 0.3, 0.8
	`skirtor2016_2`[a]	`oa`	20, 40, 60, 80
		`i`	0, 30, 60, 90
		`fracAGN`	0.1, 0.2, 0.3, 0.4, 0.5, 0.6, 0.7, 0.8, 0.9
		`EBV`	0.0, 0.05, 0.3, 0.8
X-rays	`xray`	`gam`	1.4, 1.8, 2.2, 2.6
		`alpha_ox`	−1.9, −1.7, −1.5, −1.3, −1.1

Notes. For parameters not listed here, default values have been adopted.
[a] This model is only used for dual AGN.

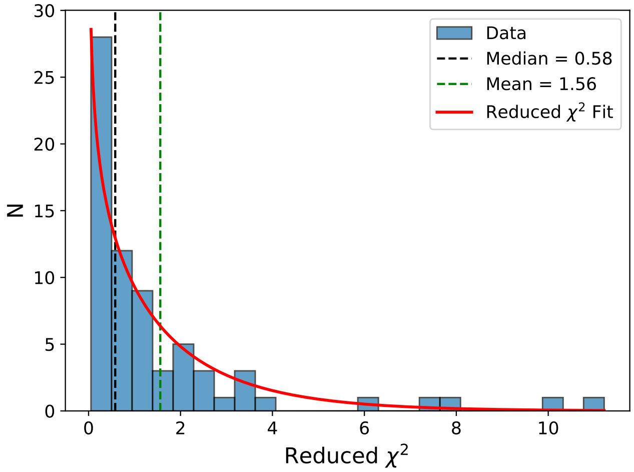

Figure 5. Reduced χ^2 distribution for the fits performed by CIGALE. The red line represents the theoretical χ^2 function for our degrees of freedom, demonstrating that our results are consistent with expectations. Furthermore, 87% of our fits have $\chi^2 < 3$ values.

data, allowing us to assess the robustness of the derived physical parameters. Overall, the values for the mock galaxies are consistent with those derived from the observed data, obtaining similar physical parameters. This consistency indicates that our results are not significantly affected by degeneracies. Further details about this procedure are provided in Appendix A.

5. Results

In this section, we present the physical properties of our sample, derived using CIGALE, as a function of the projected separation in their merging event. Figure 5 shows the reduced χ^2 distribution for our fits, with a mean of 1.56 and a median of 0.58, alongside the fitted χ^2 distribution, closely matching our results. A total of 87% of our fits have reduced $\chi^2 < 3$, indicating a high fraction of well-modeled sources. However, our mean value is higher than the expected $\chi^2 = 1$, due to the presence of a small fraction of poorly fitted sources.

Although some sources exhibit higher χ^2 values, the fraction of ∼10% bad fits is consistent with expectations from the theoretical reduced χ^2 distribution. Some poorly fitted sources ($3 < \chi^2 < 6$) are expected based on statistical predictions, and their absence would be unlikely. Our χ^2 distribution predicts ∼10 sources in this range, while we observe five. However, four sources display very large χ^2 values (>6), which is unexpected. They should instead fall within the $3 < \chi^2 < 6$ range for full consistency with the predicted distribution. The reasons for these poor fits are further discussed in Section 6.3.1. Nevertheless, our overall results closely match the theoretical distribution, which reinforces our confidence in the modeling approach employed here. The discrepancy is limited to only four sources, which is statistically negligible. Additionally, we validate our results using the mock analysis provided by CIGALE, as mentioned in Section 4. One best-fit model is presented in Figure 6, and all the SED models are in Figure Set 6.

Figure 7 shows the degree of correlation among the most important measured parameters, where redder squares indicate stronger correlations, bluer ones show stronger anticorrelation, and white represents no correlation. Distinct patterns can be observed, such as the absence of a clear correlation between the SFR and M_*, where the so-called star formation MS of galaxies might be expected for isolated sources. However, we do not find evidence of a relationship in our merger sample. In Section 6.1.1, we discuss this topic in depth. Additionally, we identify a slight anticorrelation between the SFR and the AGN

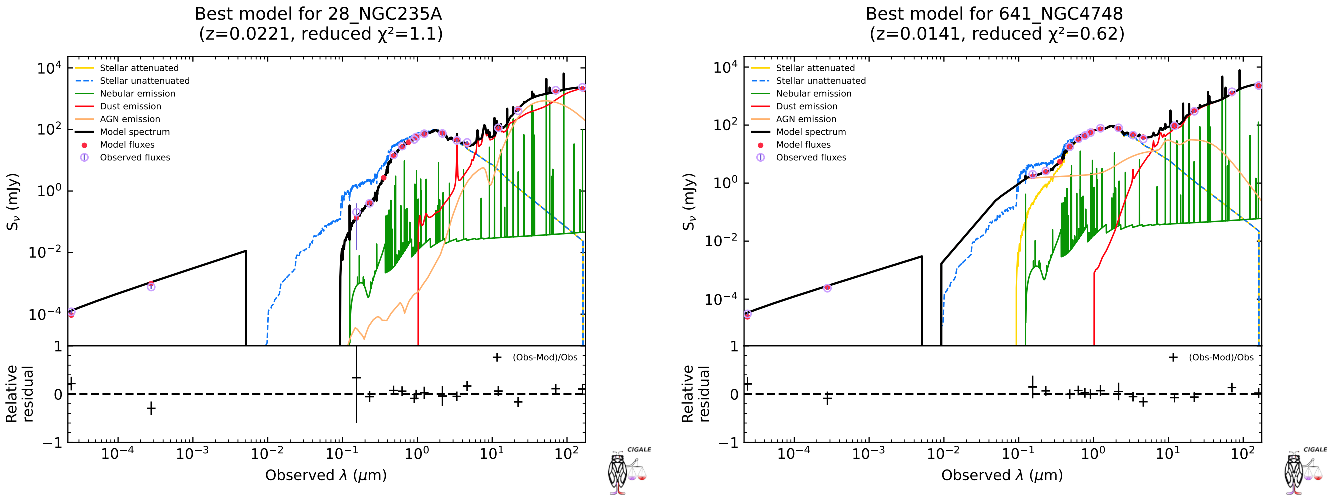

Figure 6. Best-fit SEDs for BAT ID 28 and BAT ID 641 obtained using CIGALE. Blue circles represent the observed fluxes calculated in Section 3.1, while the red circles are the model-predicted fluxes. The reduced χ^2 value quantifies the quality of each fit, and the residuals are shown in the lower panel of each subplot. (The complete figure set (70 images) is available in the online article.)

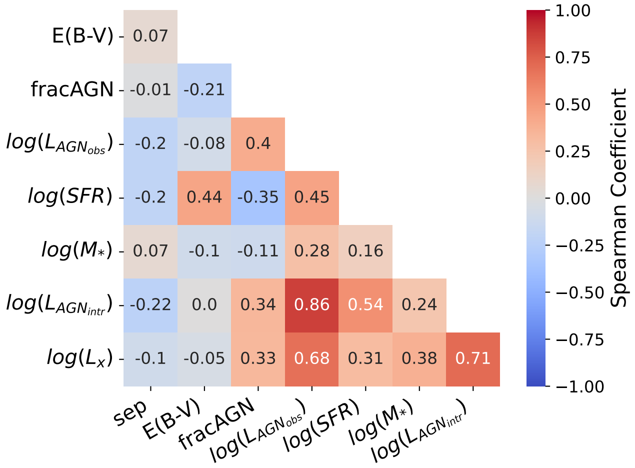

Figure 7. Confusion matrix of Spearman correlation values for pairs of physical parameters. Blue squares indicate a negative (anticorrelated) relationship, while red squares indicate a positive (correlated) relationship between the parameters.

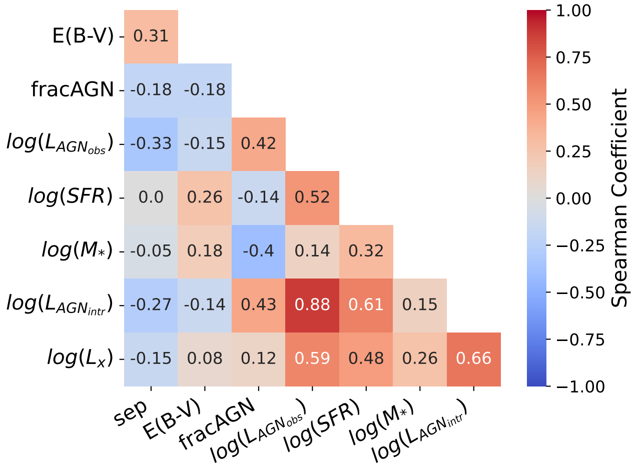

Figure 8. Confusion matrix of Spearman correlation values for pairs of physical parameters, considering only systems classified as major galaxy mergers. Colors are the same as in Figure 7.

IR luminosity fraction, suggesting possible effects from feedback caused by the more luminous AGN. Alternatively, this trend may also arise from the model's IR emission distribution, where AGN and star formation contribute, making them appear linked. Nevertheless, a mild correlation exists between the intrinsic AGN luminosity and the SFR, indicating a potential coevolution between the SMBH and the host galaxy during the merging process. Both topics are further discussed in Section 6.1.2.

5.1. Correlations for Major Mergers

We further investigate correlations between physical parameters by separating major and minor galaxy mergers, using a mass ratio of 4:1 as the dividing boundary. Figure 8 presents the correlation matrix for the physical parameters derived from our CIGALE fits, specifically considering only major galaxy mergers. Overall, there are no significant differences with the full sample, thus indicating that there are no major biases in these two samples. The only exception is the correlation between SFR and AGN luminosity, which we find is appreciably weaker in minor mergers (Spearman coefficient of 0.38), compared to the whole sample. Consequently, we can conclude that the link between star formation and AGN activity is more significant for major galaxy mergers.

5.2. Separation

The main motivation of this study is to investigate whether the physical properties of the sample are linked to the evolution of the merger process. We first use the projected nuclear separation to trace the merger stage, where smaller separations correspond to more advanced merger stages. However, as shown in the first column of Figure 7, no correlations were found between projected separation and the physical parameters of the merging systems. This lack of correlation is further illustrated in Figure 9, where the sources do not exhibit a distinct pattern or position in the diagram, at least within the observed scatter.

This nonrelation is unexpected, as simulations predict that such trends should exist (e.g., S. Byrne-Mamahit et al. 2024). First, the assumption that both galaxies in the merging system lie at the same distance from us may not hold. Since projected

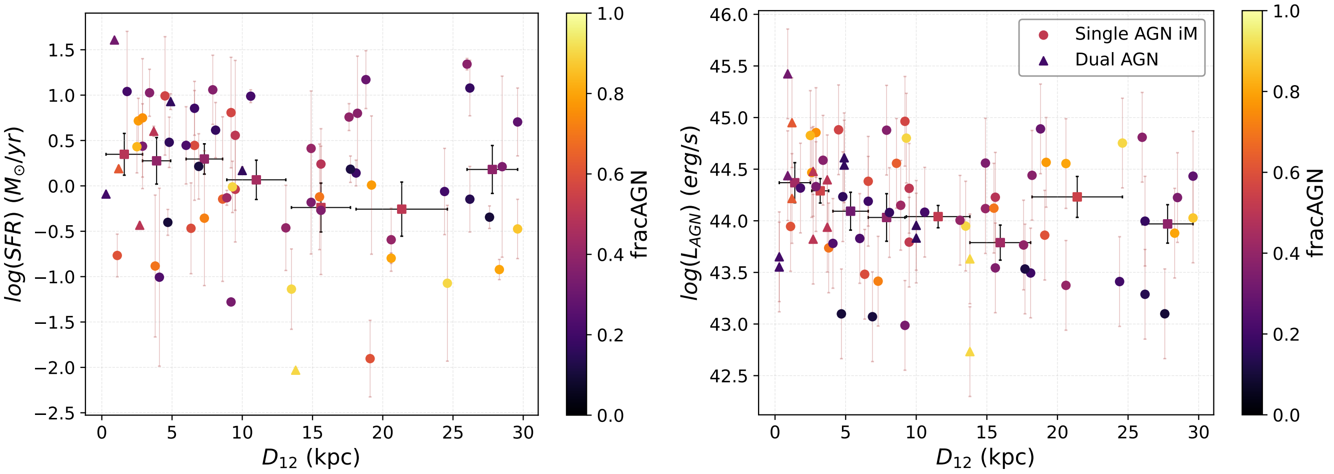

Figure 9. Left panel: SFR as a function of the projected nuclear separation. Right panel: observed total AGN luminosity as a function of nuclear separation. Both figures are colored by the fraction of AGN luminosity in the IR band. Squares represent the mean value of SFR/$L_{\rm AGN}$ in bins of nine sources.

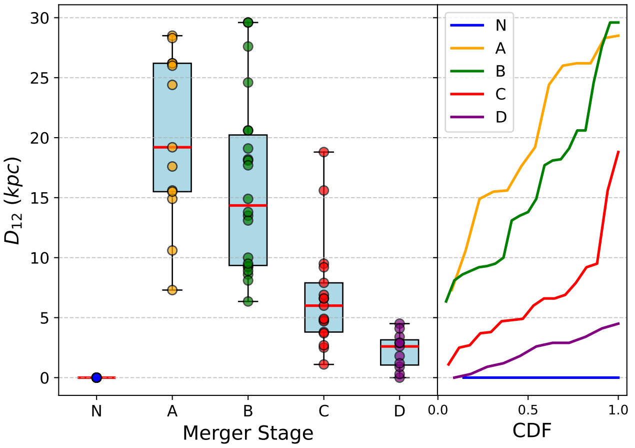

Figure 10. Projected separation as a function of the merger stage (left panel), along with the cumulative distribution function (CDF) for each stage (right panel). Nonmerging sources (N) are assigned a projected separation of 0. In the left panel, each rectangle represents the interquartile range, spanning from the first quartile (Q1) to the third quartile (Q3), while the whiskers extend to the minimum (Q0) and maximum (Q4) values within the range. The red line within each box indicates the median (Q2) of the distribution.

separations do not account for redshift differences, a merger occurring along the line of sight could potentially overestimate the merger stage. Second, galaxies can pass through each other during the merger process, resulting in an increased separation after their initial encounter (A. Toomre & J. Toomre 1972; J. E. Barnes 1988), which can lead to an underestimation of the merger stage. Hence, the lack of a strong correlation between the physical properties of the sources and their projected separation is not unexpected. Therefore, separation and morphological changes must be considered together to assess the merger stage better, as galaxies undergo significant morphological transformations throughout the merging process.

Figure 10 illustrates the relationship between projected separation and merger stage, showing a clear correlation with lower separations concentrated in the more evolved stages. However, separations often overlap, particularly in the A and B stages, which share similar separation ranges. We analyze the properties of our sources in further detail across the merger sequence in Section 6.2.

6. Discussion

In this section, using the results of our CIGALE multiwavelength SED fitting analysis, we study the interplay between AGN and their host galaxies in the context of galaxy mergers (Section 6.1). We then examine how these properties evolve throughout the merging process, using the merger stage as a proxy (Section 6.2). Finally, we discuss potential limitations and caveats of our SED fitting approach (Section 6.3.1), focusing on the effects of angular resolution differences when measuring fluxes for merging systems, the challenges of modeling dual AGN within a single SED framework, and the interpretation of fits with unusually high χ^2 values.

6.1. Coevolution of the SMBH and Host Galaxy Properties during the Merger Process

The connection between SMBHs and their host galaxies is well established (J. Kormendy & D. Richstone 1995; J. Magorrian et al. 1998; L. Ferrarese & D. Merritt 2000; K. Gebhardt et al. 2000; K. Bandara et al. 2009; K. Gültekin et al. 2009), particularly in the context of galaxy mergers (P. F. Hopkins et al. 2006; L. Blecha et al. 2018; S. Yamada et al. 2023). In this section, we compare our sample of merging galaxies to AGN-hosting systems from the BASS sample and non-AGN systems from the xCOLD GASS sample.

6.1.1. Star Formation Main Sequence

Figure 11 illustrates the position of our sample in the SFR–M_* plane. For comparison, we include a non-AGN population from xCOLD GASS (A. Saintonge et al. 2017) and the hard X-ray AGN from BASS, for which these values were previously measured (M. J. Koss et al. 2021). Our sample does not follow the local MS $\log({\rm SFR}) = 0.77 \times \log(M_*/M_\odot)$—7.53 from D. Elbaz et al. (2007), as seen in Figure 7, and as manifested by a Spearman factor of 0.16. It is important to note that the stellar mass obtained by CIGALE for our sample ranges from 10^{10} to $10^{11.5}$ $M_\odot$, following the same distribution as the BASS sample.

The distribution of our sample in the SFR–M_* plane can be divided into four distinct regions. Starting from the lower SFRs, one group is placed far below the MS (9/70),

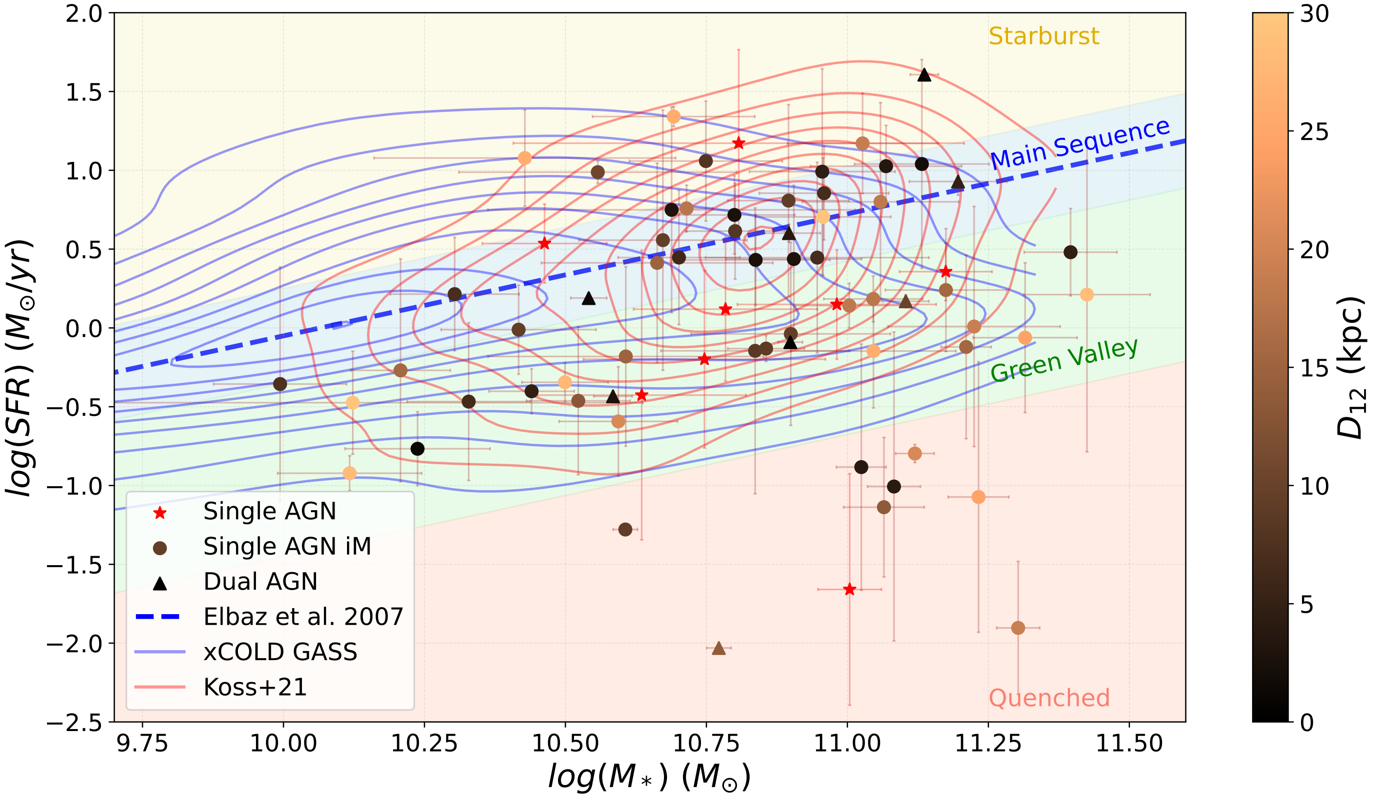

Figure 11. SFR as a function of stellar mass. The blue and red contour maps correspond to the inactive population from xCOLD GASS (A. Saintonge et al. 2017) and the active population from M. J. Koss et al. (2021), respectively. The dashed blue line marks the local star-forming MS relation from D. Elbaz et al. (2007), with the background shaded blue region representing a ±0.3 dex width scatter. Additionally, the other background shaded colors highlight different regions of the diagram: salmon for quenched galaxies, green for the green valley, and the upper yellow region for starburst galaxies. The points denote the single AGN iM, while the triangles represent the confirmed dual AGN. Both populations are colored by their projected separation. Moreover, red stars represent galaxies where only one nucleus is visible.

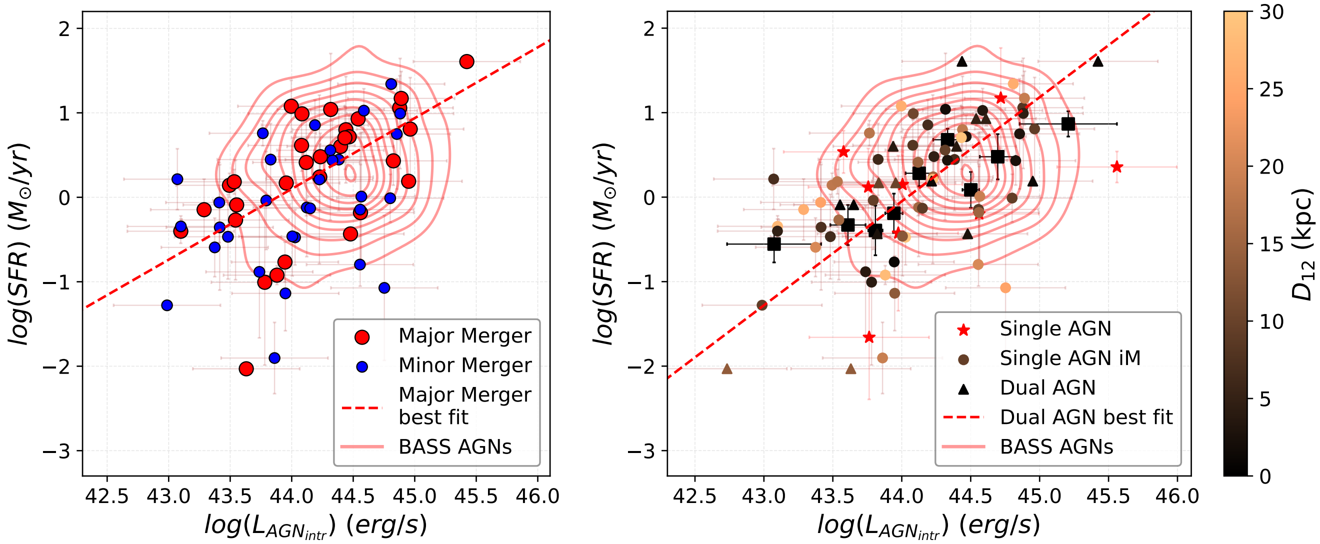

Figure 12. AGN intrinsic luminosity as a function of the SFR. Left panel: red and blue points denote major and minor galaxy mergers, respectively. Right panel: the red line corresponds to the best linear fit for the dual AGN population. Squares represent the mean value of SFR in bins of nine sources. The symbols and colors of the points are the same as in Figure 11. In both panels, the red contours represent the distribution of the sources in the BASS sample.

indicating quenched star formation. Next, a separate population appears slightly below the MS, tracing the green valley. This region (∼1.0 dex below the MS; e.g., K. Schawinski et al. 2014), where 31/70 of our sources are located, is consistent with the expectations for galaxies involved in major mergers and also with an active nucleus, as was found before for AGN in the MANGA survey (e.g., G. Jin et al. 2021). The third region lies on the MS relation, representing galaxies with normal star formation (22/70). Finally, the topmost group is found above the MS (8/70),

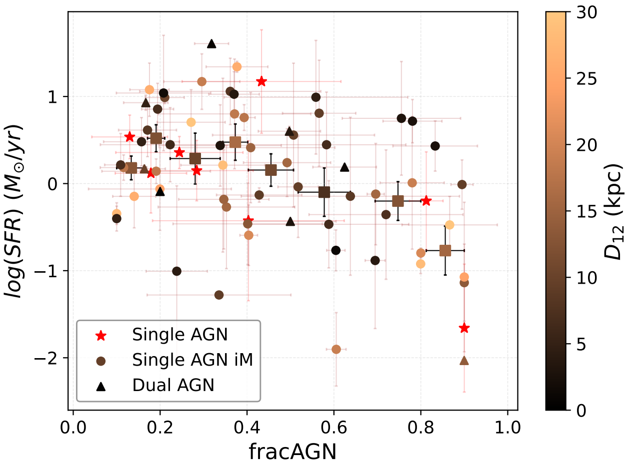

Figure 13. SFR as a function of the fraction of the AGN luminosity in the IR band. Squares represent the mean value of SFR in bins of nine sources. The symbols and colors of the points are the same as in Figure 11.

identified with starburst episodes. By number, these are less likely events, often associated with more extreme ULIRGs in the local Universe (e.g., P. Liang et al. 2024).

In nonmerging galaxies, star formation typically declines gradually over time, with fluctuations around the MS before ultimately reaching a quenched state (∼0.3 dex deviation from the MS; e.g., S. Tacchella et al. 2016). In contrast, our results suggest that galaxy mergers follow a different evolutionary path: rather than maintaining their position on the MS, many merging systems reside in the green valley throughout much of the merging process, indicating that these sources have recently undergone quenching. The distribution of our sources supports this interpretation: most of them are found in this transitional region. As shown by K. Schawinski et al. (2014), merging galaxies are indeed more likely to lie below the MS. However, they are also expected to experience a rapid starburst phase just before coalescence (ULIRGs), resulting in a subset of sources with elevated SFRs (P. F. Hopkins et al. 2008; P. Liang et al. 2024). In S. Yamada et al. (2023), using a sample of U/LIRGs from the GOALS survey, the authors reached a similar conclusion, but in the opposite direction. Mergers selected based on their IR emission exhibit elevated SFRs, with positions above the MS being the most common scenario. These apparently contradicting results highlight the impact that selection methods can have on the observed properties of the derived samples.

These results suggest that galaxy mergers can significantly alter the position of galaxies from the star-forming MS, driving them to different locations in the SFR–$M_\odot$ plane. In particular, for our AGN-merging sample, nuclear activity further complicates this picture, potentially accelerating the depletion of star-forming gas through feedback mechanisms, such as AGN-driven winds and radiative feedback (e.g., T. Di Matteo et al. 2005), pushing galaxies into the green valley before quenching is complete. To better understand this interplay, we examine the relationship between AGN properties and SFR, focusing on how AGN activity evolves during the merging process.

6.1.2. AGN Properties versus SFR

The relationship between AGN luminosity and SFR is shown in Figure 12. As indicated in Figure 7, a mild correlation is observed between these two parameters for our merging sample, with a Spearman value of 0.54. The right panel reveals that higher AGN luminosities are associated with higher SFRs in merging systems. In contrast, the nonmerging sources from the BASS sample do not exhibit a significant correlation, showing a much lower Spearman coefficient value of 0.18. When separating the mergers by mass ratio, major mergers present a stronger and more significant correlation than minor mergers, as seen in the left panel of Figure 12.

Previous studies have highlighted the connection between star formation and AGN activity (H. Netzer et al. 2007; H. Netzer 2009; B. Trakhtenbrot & H. Netzer 2010; P. Esquej et al. 2014; S. Yamada et al. 2023). However, in this hard-X-ray-selected sample, our merging galaxies and the noninteracting population from M. J. Koss et al. (2021) display distinct behaviors. The mild correlation observed in the merging systems suggests that the merger event may simultaneously drive an intense star formation episode in the host galaxy and activate the AGN. This effect is particularly evident for the major mergers in our sample, which show a stronger correlation than the minor-merger sample and the BASS nonmerging population.

Nevertheless, when the AGN dominates the IR luminosity of the galaxy, the SFR slightly decreases, as shown in Figure 13. Although this trend may partly indicate that AGN activity plays a role in quenching star formation within the host galaxy, the significant scatter in the data suggests that AGN feedback is not a dominant factor. Instead, this trend may be caused by our SED modeling approach, as the IR luminosity in the model is generated by a combination of the AGN and star formation components, which causes them to compete with each other.

The impact of AGN feedback, whether negative or positive, is now better constrained, and both mechanisms have been observed in disturbed galaxies (G. Cresci et al. 2015). This confirms that AGN activity and star formation can coexist in the same system. On the one hand, negative AGN feedback becomes significant when the AGN fraction dominates the galaxy's total IR luminosity by expelling or heating the surrounding gas. On the other hand, a higher AGN luminosity does not necessarily imply a lower SFR. In fact, in merging galaxies, we observe the opposite trend. Systems with higher AGN luminosities tend to exhibit enhanced star formation. This correlation suggests that both processes are fueled by the same gas reservoir and driven by the merger process, especially major ones, where material funneled toward the galactic center feeds the SMBH and triggers star formation in the host galaxy (P. F. Hopkins et al. 2008; S. Ellison et al. 2024, 2025; L. Ferreira et al. 2025).

6.2. Evolution of Physical Properties during the Merger Process

We employ the morphological classification outlined in Section 2.1 to properly study the merger evolution, allowing us to analyze key parameters in different merger stages. By examining the median values within each classification, we uncover trends that are not evident when individual sources are studied independently.

In terms of the evolution of the SFR, Figure 14 shows that the highest values occur in the most advanced merger stages, with a factor of 5.1 increase from stage A to stage D. Interestingly, a significant decline (factor of 0.56) is observed

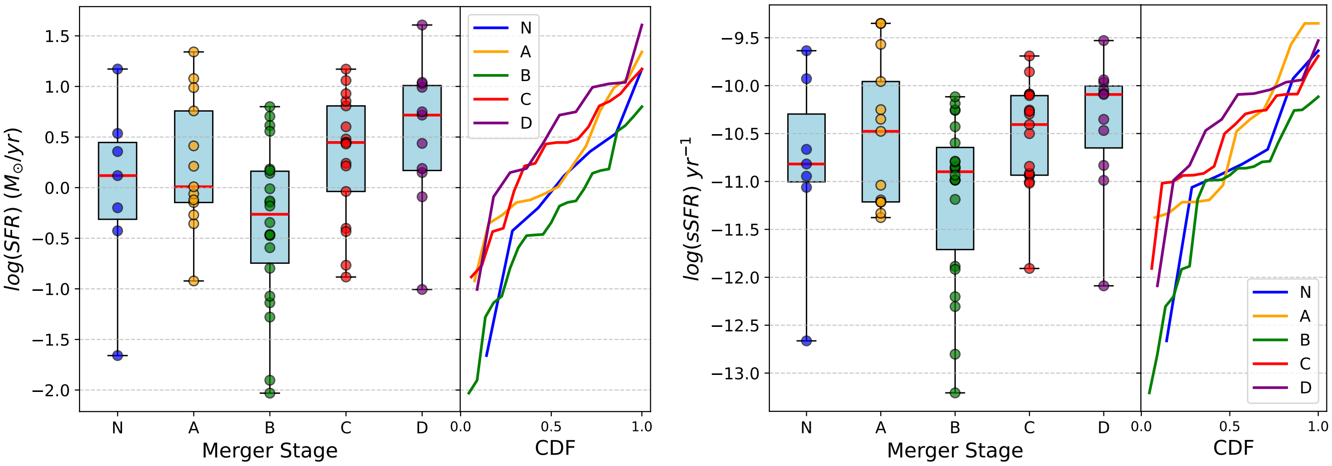

Figure 14. Left panel: SFR as a function of the merger stage. Right panel: specific SFR as a function of the merger stage, along with the cumulative distribution function (CDF) for each stage. Symbols are the same as those defined in Figure 10.

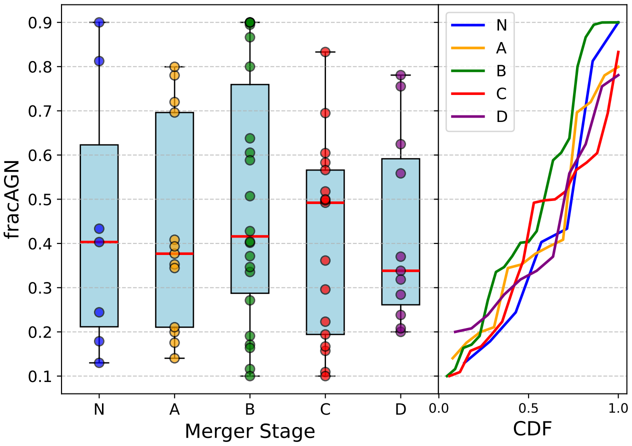

Figure 15. Fraction of the AGN luminosity in the IR band as a function of the merger stage, along with the cumulative distribution function (CDF) for each stage. Symbols are the same as those defined in Figure 10.

between pre-stage mergers and early-stage mergers. Although this phenomenon could be a genuine physical property of this stage, no other studies have found a similar behavior supporting this result. Moreover, inspection of the plot reveals that the most densely populated values are consistent between stages A and B, with the observed drop largely driven by two outliers with exceptionally low SFRs.

The dominance of the AGN in the IR luminosity shows no clear correlation with the merger stage, as illustrated in Figure 15. This suggests that the merging process does not significantly impact the ratio between AGN luminosity and SFR, with a wide range of values observed across all stages. In particular, we observe systems ranging from AGN dominated to star formation dominated at every merger stage, indicating that this ratio remains largely unaffected by the merger progression. Interestingly, in stage D we see a possible drop in the AGN dominance. This could be consistent with a "blowout" phase, where powerful AGN feedback clears the nuclear region of gas and dust. However, given the limited statistics, we cannot confirm this interpretation, and we therefore leave it as a possibility.

Particularly in the D stage, we can observe a possible drop, which could correspond to a blowout phase, evacuating the nuclear region and pushing the star formation in the outskirts. However, we do not have the necessary evidence to state it, so we left it there as a caveat.

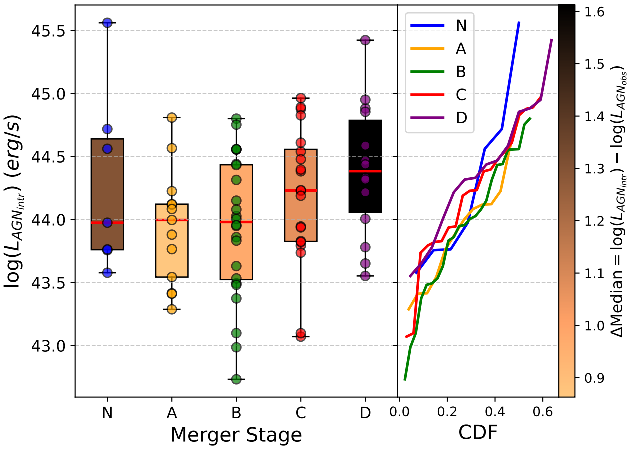

Figure 16. AGN intrinsic disk luminosity as a function of the merger stage. Each box is colored by the difference between the median AGN intrinsic disk luminosity and the median AGN observed disk luminosity. Symbols are the same as those defined in Figure 10.

However, the luminosity due to the AGN accretion disk presents a trend with the merger stage, as shown in Figure 16. On average, the luminosity progressively increases with more advanced merger stages, exhibiting a 2.4-fold increase from stage A to stage D, which indicates that the merger process accelerates the nuclear accretion rate. This result is consistent with theoretical expectations and has been previously reported in various observational studies (M. Koss et al. 2012; S. Yamada et al. 2023) and simulations (P. R. Capelo et al. 2015; A. Bhattacharya et al. 2023). Additionally, the color-coded plot highlights the difference between the intrinsic and observed disk AGN luminosity, revealing that more evolved merger stages are associated with higher extinction levels by a factor of 2.8, as previously reported by C. Ricci et al. (2017a, 2021).

As shown in the figures described above, the AGN luminosity and the SFR increase in the final stages of the mergers. The most significant difference between the early stages (A and B) and the late stages (C and D) is the degree of

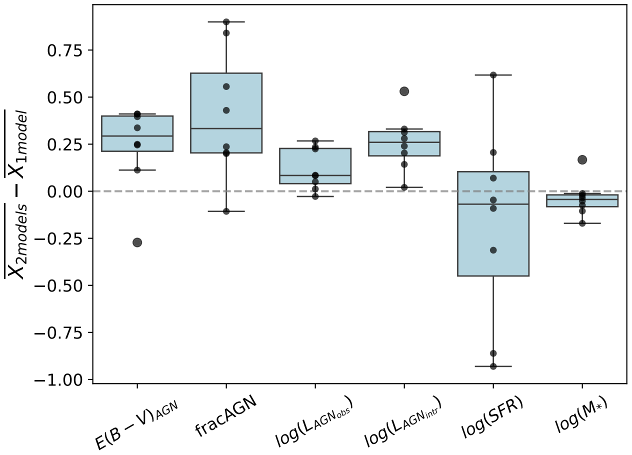

Figure 17. Comparison of physical properties of dual AGN measured using one vs. two AGN components. Each point represents the difference between the values obtained with two AGN components and those derived from a single-component model. For AGN luminosities in the two-component model, the total value corresponds to the sum of both luminosities.

disturbance in their disks (S. Stierwalt et al. 2013), which likely triggers both processes. This suggests that the same mechanism fuels star formation and black hole accretion as the merger progresses, driving the system toward its final shape and structure.

6.3. SED Fitting Results

In this section, we discuss the implications of the SED fitting methodology for our analysis, particularly the impact of using merging galaxies in an SED fitting code (Section 6.3.1), and provide a more detailed study of the poorer fits in our sample (Section 6.3.2).

6.3.1. Impact of Angular Resolution Differences in the Merger's SED

As discussed in Section 3.1, resolving both galaxies individually for SED fitting is not feasible in our study owing to the limitation of the spatial resolution of bands such as WISE W4 and PACS. Consequently, we derive the physical parameters for the two galaxies as a single system. This approach has been employed in previous studies. In particular, S. Yamada et al. (2023) quantified the impact of merging two galaxies into a single SED fit for nonactive systems and single AGN in mergers. Their findings indicate that while the host galaxy properties remain unchanged, the AGN luminosities differ by approximately 0.2 dex, a small effect that is unlikely to impact our results significantly.

Roughly, this method produces a luminosity-weighted average of both galaxies; however, its effects on the physical parameters derived from the SED fitting may depend on the merger stage. In the less evolved mergers (A and B stages), where both disks remain independent, the individual properties of each galaxy may still influence the results. However, their physical properties would be mixed in later stages (C and D), where the disks have already merged.

From the AGN perspective, single AGN in mergers are unlikely to be affected, given that we model only a single AGN. However, for confirmed dual AGN, applying a single-component AGN fit could introduce inaccuracies owing to their potentially distinct characteristics, such as varying levels of obscuration, accretion rates, and torus geometries. As presented in Section 4, we address this issue by incorporating two AGN components in CIGALE for a more realistic modeling of the combined SED, and we present an example of this approach in Appendix B. Figure 17 illustrates the impact of using a single-component AGN model instead of two separate AGN components. In general, SFR tends to be overestimated, whereas the AGN properties are underestimated in the single-component model. This is due to degeneracies in IR emission, where SFR and AGN luminosity both contribute in a similar wavelength range. Nevertheless, our multiwavelength approach must address this issue, particularly through X-ray observations, which may help determine the intrinsic AGN luminosity for most sources. Given this, the overall differences remain minimal.

Including longer-wavelength fluxes would further improve the SED fitting by extending the coverage. Nevertheless, T. Kawamuro et al. (2022) found a strong correlation between X-ray and millimeter emission in the BASS sample, suggesting that additional data in that range may not be necessary for our study, given that the information is already there. Moreover, radio data might be complicated owing to the radio-loud/radio-quiet dichotomy (S. Zamfir et al. 2008; M. Baloković et al. 2012), and hence such a study, incorporating radio data, is beyond the scope of this work.

In the near future, repeating this analysis at higher spatial resolutions across the entire wavelength range, particularly in the IR using telescopes such as JWST, would be the most effective way to separate the emission from the participating galaxies. Currently, however, no instruments cover the range between 30 and 400 μm with the required spatial resolution to separate galaxies at projected distances below ∼12″ (WISE W4 resolution) and ideally resolve nuclear regions, as achieved in the UV, optical, and NIR with HST, JWST, AO ground-based imaging, or even in X-rays with Chandra. This limitation implies that we must wait for future observational capabilities to fully resolve these systems spatially in the entire wavelength spectrum.

6.3.2. Analysis of Fits with Large Residuals

In Section 5, we identified four sources with exceptionally large χ^2 values that deviate significantly from the expected distribution. Their SEDs are presented in Figure 6. These poor fits likely arise from systematic issues. For BAT ID 13 and BAT ID 489, we suspect that the high χ^2 values result from template incompleteness, as neither source exhibits unusual behavior, and no specific filter dominates the residuals. BAT ID 72 has the highest χ^2 and is classified as a dual AGN. While its fluxes follow a consistent shape, the model fails to reach the required luminosity, even when incorporating two AGN components. Since the X-ray bands primarily constrain AGN luminosity, the observed IR flux deficit may indicate that the relatively bad fit can be due to an incomplete template for the star formation parameters. Finally, BASS ID 329 has most of its χ^2 arising in the NUV filter, suggesting that the poor fit may be due to inaccurate photometry in that band.

7. Conclusions

Using a sample of 72 AGN-hosting galaxy mergers from BASS, we conducted SED fitting with self-measured fluxes with homogeneous apertures across all the included filters, spanning from X-rays to FIR. This multiwavelength approach ensures consistency across the entire spectral range, allowing us to accurately constrain the physical properties of both the host galaxies and their central SMBHs throughout the merger process. Our study provides new insights into the interplay between AGN activity, star formation, and the evolution of merging systems in the context of local Universe ($z < 0.1$) AGN. The main conclusions of our analysis are as follows:

1. Merging galaxies with active nuclei are not predominantly found around the star-forming MS. Instead, they span all possible cases: quenched systems, green valley, MS, and starburst galaxies. Most systems are found below the MS, in the green valley region.
2. The merger process can enhance AGN activity and star formation, finding a correlation between these two physical parameters for our interacting systems. We also find an opposite scenario for nonmerging AGN, which do not present a clear connection. This trend is expected since these sources are mainly fueled by stochastic processes.
3. The strength of the AGN–star formation relation depends on the merger mass ratio, where major mergers show a clear correlation between AGN luminosity and SFR, whereas minor mergers do not. This highlights the critical role of major galaxy mergers in setting up the connection between SMBH growth and galaxy evolution.
4. The dominance of the AGN at IR wavelengths could suggest a quenching of star formation. However, this trend may be driven by our SED fitting approach, where the IR luminosity is distributed between the AGN and star formation components, leading to a competition between them.
5. The projected nuclear separation is not necessarily a reliable tracer of the merger stage. Instead, other tracers, such as visual studies of morphological features, can help to assess the coalescence stage.
6. Incorporating this morphological analysis, we find that late-stage mergers present higher SFR, AGN luminosity, and obscuration, supporting the idea that the final stages of mergers enhance the SMBH growth along with the host galaxy evolution.
7. Fitting two AGN with only one component generates discrepancies in the accretion rate and SFR in the galaxy. Using two components obtains more consistent values, making the results more reliable.

Our work indicates that galaxies undergoing a merger process experience significant changes in their physical properties, which continue to evolve as the merger progresses. Future studies at relatively long wavelengths will require high angular resolution observations to gain deeper insights into the role of mergers in shaping the coevolution of SMBHs and their host galaxies. Separately resolving both merging components will be essential to understanding the individual contributions of each galaxy to the overall system, particularly in the final stages of the coalescence.

Acknowledgments

We thank the anonymous referee for a very positive and constructive review that, in our opinion, significantly improved the quality and presentation of this article. M.T., E.T., A.R., M.B., F.E.B., R.J.A., and C.R. acknowledge support from the ANID CATA-BASAL program FB210003. E.T. and F.E.B. acknowledge support from FONDECYT Regular—1190818, 1200495, 1241005, and 1250821. F.E.B. acknowledges support from the ANID Millennium Science Initiative Program ICN12_009. E.T. would like to acknowledge the hospitality of the North American ALMA Science Center (NAASC) at NRAO during his sabbatical stay in 2022, where a significant fraction of this work was carried out. M.K. acknowledges support from NASA through ADAP award 80NSSC22K1126. This work was initiated in part at the Aspen Center for Physics, which is supported by National Science Foundation grant PHY-2210452. I.M.C. acknowledges support from the FONDECYT Postdoctorado program 3230653. C.R. acknowledges support from Fondecyt Regular grant 1230345 and the China-Chile joint research fund. M.B. acknowledges support from the French government through the France 2030 investment plan managed by the National Research Agency (ANR), as part of the Initiative of Excellence of Université Côte d'Azur under reference No. ANR-15-IDEX-01. R.J.A. was supported by FONDECYT grant No. 1231718. K.O. acknowledges support from the Korea Astronomy and Space Science Institute under the R&D program (project No. 2025-1-831-01), supervised by the Korea AeroSpace Administration, and the National Research Foundation of Korea (NRF) grant funded by the Korea government (MSIT; RS-2025-00553982). M.S. acknowledges financial support from the Italian Ministry for University and Research, through the grant PNRR-M4C2-I1.1-PRIN 2022-PE9-SEAWIND: Super-Eddington Accretion: Wind, INflow and Disk-F53D23001250006-NextGenerationEU.

Appendix A
Mock Analysis

To test the robustness of our results, we performed a mock analysis to evaluate potential degeneracies in the derived physical properties. Figure A1 presents the outcome of this analysis, including the 1:1 relation, the 3σ range, and the best-fit linear regression. The AGN luminosities show a strong and tight correlation, with a 1:1 line and the best-fit line overlapping and with no outliers outside the 3σ interval. Regarding the SFR, it also exhibits low scatter and closely follows the 1:1 relation. In contrast, the M_* shows two outliers beyond the 3σ range, which affects the quality of the fit, though the overall scatter remains small. The AGN fraction follows the expected trend but with a higher scatter. Finally, the AGN obscuration presents the highest dispersion and a less significant fit, suggesting possible degeneracies in these measurements. Nevertheless, most points still lie close to the 1:1 relation, supporting the overall reliability of the fitting process.

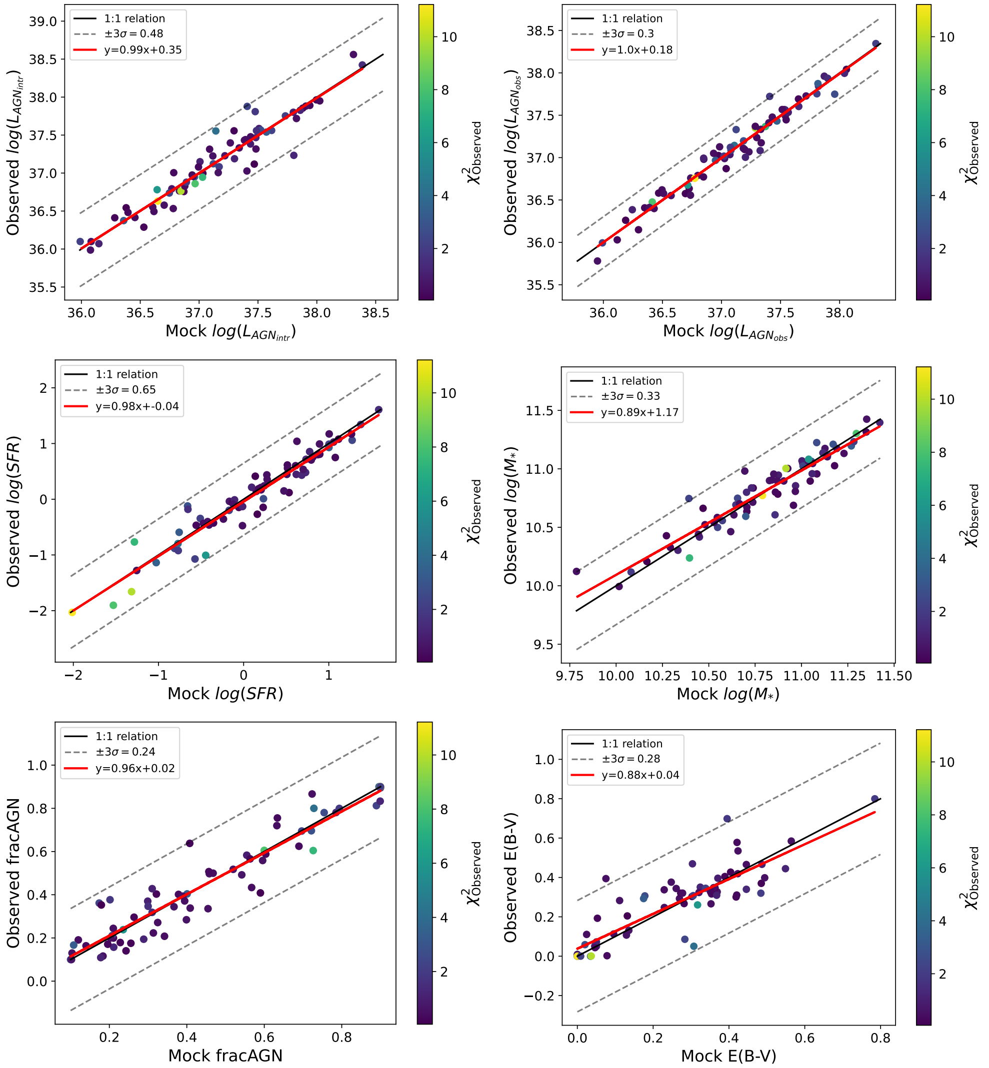

Figure A1. Mock analysis for the key physical parameters used in this study. The *x*-axis shows the values recovered with the mock fluxes, while the *y*-axis displays the values obtained from the observed SEDs. Each point is colored by the reduced χ^2 value of the observed fit. The black diagonal line indicates the 1:1 relation, the red line shows the best linear fit, and the dashed lines show the 3σ range.

Appendix B
Dual AGN SED

We applied the two-AGN model approach to the eight confirmed dual AGN (excluding the ninth dual AGN, BAT ID 497, which did not converge to a reliable solution). On average, the fits improve by 49% with standard deviation of 14%. As an illustrative example, Figure B1 shows the case of BAT ID 841, where the two-AGN fit achieves lower reduced χ^2 compared to the one-AGN model, while keeping the same host galaxy parameters fixed.

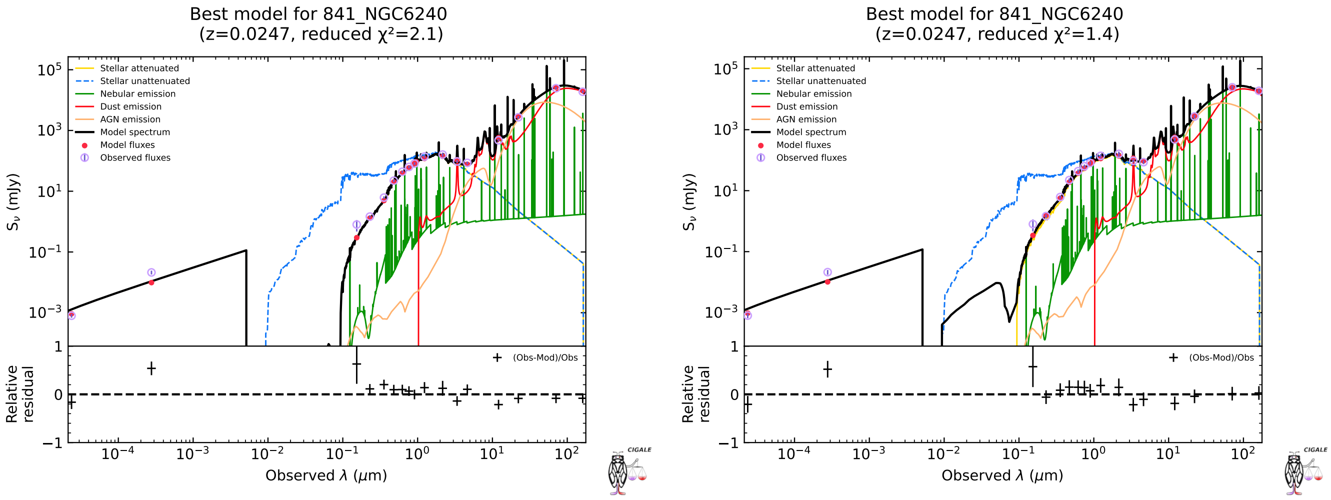

Figure B1. Best-fit SED for BAT ID 841 using a one-AGN model (left) and a two-AGN model (right). The two-AGN model provides a better fit while preserving the same host galaxy parameters.

ORCID iDs

Marco Troncoso https://orcid.org/0009-0002-2740-2993
Ezequiel Treister https://orcid.org/0000-0001-7568-6412
Alejandra Rojas https://orcid.org/0000-0003-0006-8681
Médéric Boquien https://orcid.org/0000-0003-0946-6176
Franz Bauer https://orcid.org/0000-0002-8686-8737
Michael J. Koss https://orcid.org/0000-0002-7998-9581
Roberto J. Assef https://orcid.org/0000-0002-9508-3667
Miguel Parra Tello https://orcid.org/0000-0001-5649-7798
Ignacio del Moral-Castro https://orcid.org/0000-0001-8931-1152
Claudio Ricci https://orcid.org/0000-0001-5231-2645
Sophia Dai https://orcid.org/0000-0002-7928-416X
Kyuseok Oh https://orcid.org/0000-0002-5037-951X
Federica Ricci https://orcid.org/0000-0001-5742-5980
Alessandro Peca https://orcid.org/0000-0003-2196-3298
C. Megan Urry https://orcid.org/0000-0002-0745-9792
Kriti Kamal Gupta https://orcid.org/0009-0007-9018-1077
Giacomo Venturi https://orcid.org/0000-0001-8349-3055
Matilde Signorini https://orcid.org/0000-0002-8177-6905
Richard Mushotzky https://orcid.org/0000-0002-7962-5446
David Sanders https://orcid.org/0000-0002-1233-9998

References

Abbott, T. M. C., Abdalla, F. B., Allam, S., et al. 2018, ApJS, 239, 18
Ananna, T. T., Weigel, A. K., Trakhtenbrot, B., et al. 2022, ApJS, 261, 9
Baloković, M., Smolčić, V., Ivezić, Ž., et al. 2012, ApJ, 759, 30
Bandara, K., Crampton, D., & Simard, L. 2009, ApJ, 704, 1135
Barnes, J. E. 1988, ApJ, 331, 699
Barnes, J. E., & Hernquist, L. E. 1991, ApJL, 370, L65
Baumgartner, W. H., Tueller, J., Markwardt, C. B., et al. 2013, ApJS, 207, 19
Bhattacharya, A., Nehal, C. P., Das, M., et al. 2023, MNRAS, 524, 4482
Blecha, L., Snyder, G. F., Satyapal, S., & Ellison, S. L. 2018, MNRAS, 478, 3056
Boquien, M., Burgarella, D., Roehlly, Y., et al. 2019, A&A, 622, A103
Bruzual, G., & Charlot, S. 2003, MNRAS, 344, 1000
Byrne-Mamahit, S., Patton, D. R., Ellison, S. L., et al. 2024, MNRAS, 528, 5864
Calzetti, D., Armus, L., Bohlin, R. C., et al. 2000, ApJ, 533, 682
Capelo, P. R., Volonteri, M., Dotti, M., et al. 2015, MNRAS, 447, 2123
Comerford, J. M., Griffith, R. L., Gerke, B. F., et al. 2009, ApJL, 702, L82
Conselice, C. J. 2006, ApJ, 638, 686
Cresci, G., Mainieri, V., Brusa, M., et al. 2015, ApJ, 799, 82
Dey, A., Schlegel, D. J., Lang, D., et al. 2019, AJ, 157, 168
Di Matteo, P., Bournaud, F., Martig, M., et al. 2008, A&A, 492, 31
Di Matteo, T., Springel, V., & Hernquist, L. 2005, Natur, 433, 604
Díaz-Santos, T., Assef, R. J., Blain, A. W., et al. 2018, Sci, 362, 1034
Diemer, B., Sparre, M., Abramson, L. E., & Torrey, P. 2017, ApJ, 839, 26
Draine, B. T., Aniano, G., Krause, O., et al. 2014, ApJ, 780, 172
Edelson, R. A., & Malkan, M. A. 1986, ApJ, 308, 59
Elbaz, D., Daddi, E., Le Borgne, D., et al. 2007, A&A, 468, 33
Elbaz, D., Dickinson, M., Hwang, H. S., et al. 2011, A&A, 533, A119
Ellison, S., Ferreira, L., Bickley, R., et al. 2025, OJAp, 8, 12
Ellison, S., Ferreira, L., Wild, V., et al. 2024, OJAp, 7, 121
Ellison, S. L., Patton, D. R., Mendel, J. T., & Scudder, J. M. 2011, MNRAS, 418, 2043
Ellison, S. L., Patton, D. R., Simard, L., & McConnachie, A. W. 2008, AJ, 135, 1877
Ellison, S. L., Viswanathan, A., Patton, D. R., et al. 2019, MNRAS, 487, 2491
Esquej, P., Alonso-Herrero, A., González-Martín, O., et al. 2014, ApJ, 780, 86
Fan, L., Han, Y., Fang, G., et al. 2016, ApJL, 822, L32
Ferrarese, L., & Merritt, D. 2000, ApJL, 539, L9
Ferreira, L., Ellison, S. L., Patton, D. R., et al. 2025, MNRAS, 538, L31
Fu, H., Steffen, J. L., Gross, A. C., et al. 2018, ApJ, 856, 93
Gaia Collaboration, Vallenari, A., Brown, A. G. A., et al. 2023, A&A, 674, A1
Gebhardt, K., Bender, R., Bower, G., et al. 2000, ApJL, 539, L13
Green, G. 2018, JOSS, 3, 695
Gültekin, K., Richstone, D. O., Gebhardt, K., et al. 2009, ApJ, 698, 198
Harrison, F. A., Aird, J., Civano, F., et al. 2016, ApJ, 831, 185
Hernández-Toledo, H. M., Avila-Reese, V., Conselice, C. J., & Puerari, I. 2005, AJ, 129, 682
Hopkins, P. F., Hernquist, L., Cox, T. J., et al. 2006, ApJS, 163, 1
Hopkins, P. F., Hernquist, L., Cox, T. J., & Kereš, D. 2008, ApJS, 175, 356
Hopkins, P. F., & Quataert, E. 2011, MNRAS, 415, 1027
Iguchi, S., Morita, K.-I., Sugimoto, M., et al. 2009, PASJ, 61, 1
Jin, G., Dai, Y. S., Pan, H.-A., et al. 2021, ApJ, 923, 6
Kawamuro, T., Ricci, C., Imanishi, M., et al. 2022, ApJ, 938, 87
Kormendy, J., & Richstone, D. 1995, ARA&A, 33, 581
Koss, M., Mushotzky, R., Treister, E., et al. 2012, ApJL, 746, L22
Koss, M., Mushotzky, R., Veilleux, S., et al. 2011, ApJ, 739, 57
Koss, M., Mushotzky, R., Veilleux, S., & Winter, L. 2010, ApJL, 716, L125
Koss, M. J., Blecha, L., Bernhard, P., et al. 2018, Natur, 563, 214
Koss, M. J., Ricci, C., Trakhtenbrot, B., et al. 2022a, ApJS, 261, 2
Koss, M. J., Strittmatter, B., Lamperti, I., et al. 2021, ApJS, 252, 29
Koss, M. J., Trakhtenbrot, B., Ricci, C., et al. 2022b, ApJS, 261, 1
La Marca, A., Margalef-Bentabol, B., Wang, L., et al. 2024, A&A, 690, A326
Liang, P., Dai, Y. S., Huang, J.-S., Cheng, C., & Shi, Y. 2024, ApJ, 970, 29
Lynden-Bell, D. 1969, Natur, 223, 690
Magorrian, J., Tremaine, S., Richstone, D., et al. 1998, AJ, 115, 2285
Martin, D. C., Fanson, J., Schiminovich, D., et al. 2005, ApJL, 619, L1
McGregor, P., Hart, J., Stevanovic, D., et al. 2004, Proc. SPIE, 5492, 1033
Mechtley, M., Jahnke, K., Windhorst, R. A., et al. 2016, ApJ, 830, 156
Mihos, J. C., & Hernquist, L. 1996, ApJ, 464, 641

Netzer, H. 2009, MNRAS, 399, 1907
Netzer, H., Lira, P., Trakhtenbrot, B., Shemmer, O., & Cury, I. 2007, ApJ, 671, 1256
Oh, K., Koss, M., Markwardt, C. B., et al. 2018, ApJS, 235, 4
Patton, D. R., Torrey, P., Ellison, S. L., Mendel, J. T., & Scudder, J. M. 2013, MNRAS, 433, L59
Pfeifle, R. W., Satyapal, S., Secrest, N. J., et al. 2019, ApJ, 875, 117
Pfeifle, R. W., Weaver, K., Secrest, N., Rothberg, B., & Patton, D. 2025, AAS, 57, 140.03
Poglitsch, A., Waelkens, C., Geis, N., et al. 2010, A&A, 518, L2
Polletta, M., Tajer, M., Maraschi, L., et al. 2007, ApJ, 663, 81
Reeves, A. M. M., & Hudson, M. J. 2024, MNRAS, 527, 2037
Ricci, C., Bauer, F. E., Treister, E., et al. 2017a, MNRAS, 468, 1273
Ricci, C., Privon, G. C., Pfeifle, R. W., et al. 2021, MNRAS, 506, 5935
Ricci, C., Trakhtenbrot, B., Koss, M. J., et al. 2017b, ApJS, 233, 17
Ricci, C., Ueda, Y., Koss, M. J., et al. 2015, ApJL, 815, L13
Rodighiero, G., Daddi, E., Baronchelli, I., et al. 2011, ApJL, 739, L40
Saintonge, A., Catinella, B., Tacconi, L. J., et al. 2017, ApJS, 233, 22
Sanders, D. B., Soifer, B. T., Elias, J. H., et al. 1988, ApJ, 325, 74
Satyapal, S., Ellison, S. L., McAlpine, W., et al. 2014, MNRAS, 441, 1297
Schawinski, K., Koss, M., Berney, S., & Sartori, L. F. 2015, MNRAS, 451, 2517
Schawinski, K., Urry, C. M., Simmons, B. D., et al. 2014, MNRAS, 440, 889
Schirmer, M. 2013, ApJS, 209, 21
Schlafly, E. F., & Finkbeiner, D. P. 2011, ApJ, 737, 103
Schreiber, C., Pannella, M., Elbaz, D., et al. 2015, A&A, 575, A74
Scudder, J. M., Ellison, S. L., Torrey, P., Patton, D. R., & Mendel, J. T. 2012, MNRAS, 426, 549
Skrutskie, M. F., Cutri, R. M., Stiening, R., et al. 2006, AJ, 131, 1163
Springel, V., Di Matteo, T., & Hernquist, L. 2005, ApJL, 620, L79
Stalevski, M. 2012, BlgAJ, 18, 3
Stemo, A., Comerford, J. M., Barrows, R. S., et al. 2021, ApJ, 923, 36
Stierwalt, S., Armus, L., Surace, J. A., et al. 2013, ApJS, 206, 1
Tacchella, S., Dekel, A., Carollo, C. M., et al. 2016, MNRAS, 457, 2790
Toomre, A., & Toomre, J. 1972, ApJ, 178, 623
Trakhtenbrot, B., & Netzer, H. 2010, MNRAS, 406, L35
Treister, E., Schawinski, K., Urry, C. M., & Simmons, B. D. 2012, ApJL, 758, L39
Van Wassenhove, S., Volonteri, M., Mayer, L., et al. 2012, ApJL, 748, L7
Veilleux, S., Kim, D. C., & Sanders, D. B. 2002, ApJS, 143, 315
Wold, M., Brotherton, M. S., & Shang, Z. 2007, MNRAS, 375, 989
Wright, E. L., Eisenhardt, P. R. M., Mainzer, A. K., et al. 2010, AJ, 140, 1868
Yamada, S., Ueda, Y., Herrera-Endoqui, M., et al. 2023, ApJS, 265, 37
Yang, G., Boquien, M., Brandt, W. N., et al. 2022, ApJ, 927, 192
Yang, G., Boquien, M., Buat, V., et al. 2020, MNRAS, 491, 740
York, D. G., Adelman, J., Anderson, J. E., Jr., et al. 2000, AJ, 120, 1579
Yuan, H. B., Liu, X. W., & Xiang, M. S. 2013, MNRAS, 430, 2188
Zakamska, N. L., Sun, A.-L., Strauss, M. A., et al. 2019, MNRAS, 489, 497
Zamfir, S., Sulentic, J. W., & Marziani, P. 2008, MNRAS, 387, 856